Forced bars induced by variations of channel width: Implications for incipient bifurcation

Fu-Chun Wu[1] and Tzu-Hao Yeh

Department of Bioenvironmental Systems Engineering, National Taiwan University, Taipei, Taiwan

Received 22 April 2004; revised 28 January 2005; accepted 21 February 2005; published 18 May 2005.

[1] In this study we investigate forced bars that form in a channel with periodic width variations. A depth-averaged two-dimensional (2-D) model incorporating a simplified correction for the helical flows induced by streamline curvature is used to obtain analytical solution of bed deformation. Flume experiments are conducted to verify the model results. With the correction included, the 2-D model will be comparable to the 3-D model. Because the no-slip condition is relaxed at the sidewalls, the model gives distorted results in the near-bank region, particularly at narrow sections, but the bed topography is satisfactory for the major part of the channel. The forced bars are classified into four types according to the locations of peak deformations. Transition from one type to another is controlled mainly by the aspect ratio β. Increasing the value of β exhibits sequentially the purely central bars (mode 1), transverse bars (central mode 1), side bars, and transverse bars (central mode 2). The analytical solution is used to derive a criterion for central bar formation, which implies a condition required for incipient bifurcation. Given the bank profile, flow, and sediment conditions, the central bars of mode 1 would develop for $\beta < \beta_{c1}$ (a lower critical value), the central bars of mode 2 would develop for $\beta > \beta_{c2}$ (an upper critical value), whereas side bars would form for $\beta_{c1} < \beta < \beta_{c2}$. Such criteria for formation of different bar patterns are necessary but not sufficient conditions for establishing stable regimes.

Citation: Wu, F.-C., and T.-H. Yeh (2005), Forced bars induced by variations of channel width: Implications for incipient bifurcation, *J. Geophys. Res.*, *110*, F02009, doi:10.1029/2004JF000160.

1. Introduction

[2] Variations of channel width constitute a typical characteristic of natural river planforms, which may manifest a certain degree of regularity. In straight channels, width variations may arise from bank erosion induced by bar development. In meandering channels, width variations follow curvature variations. In braided rivers, a network of interlaced channels display considerable variations in width, both of the individual channel segments and of the whole channel ensemble [*Tubino et al.*, 1999; *Repetto et al.*, 2002]. The geomorphic processes of alluvial channels are essentially governed by the interaction between free and forced bed forms. The former, typically in a pattern of migrating alternate bars, spontaneously develop in the channel as a result of an inherent instability of the flow-sediment system [*Callander*, 1969, 1978; *Colombini et al.*, 1987]. The latter, typically in the form of steady (or stationary) bars, are induced by forcing effects such as channel curvature and width variations [*Seminara and Tubino*, 1989; *Repetto et al.*, 2002]. Under a sufficiently strong forcing effect, it has been observed in many cases that migrating free bars would be suppressed [e.g., *Kinoshita and Miwa*, 1974; *Tubino and Seminara*, 1990; *García and Niño*, 1993], leading to a steady bed configuration that in turn may affect the planimetric channel evolution.

[3] The forcing effect of channel curvature and formation of point bars have been extensively investigated over the last three decades [e.g., *Kikkawa et al.*, 1976; *Ikeda and Nishimura*, 1985; *Seminara and Tubino*, 1989; *Parker and Johannesson*, 1989; *Whiting and Dietrich*, 1993; *Seminara et al.*, 2001, and references therein], primarily due to its natural association with the development of river meanders. In contrast, the forcing effect of width variations has received much less attention. Existing predictive models of river morphodynamics have almost entirely depended upon the assumption of constant width, except a few such as that developed by *Darby et al.* [2002]. Two recent studies conducted by *Bittner* [1994] and *Repetto* [2000] using laboratory channels with periodic width variations have demonstrated significant differences in bed topography as compared to the results observed in channels with constant width. Under stable regimes (i.e., in the absence of alternate bars), the steady bed profiles that developed in their channels consist of a consistent longitudinal deformation pattern with the deposition and scour occurring at the wide and narrow sections, respectively. The transverse bed configurations at the wide sections, however, were not consistent in all runs, they

[1] Also at Hydrotech Research Institute, National Taiwan University, Taipei, Taiwan.

0148-0227/05/2004JF000160$09.00

Table 1. Available Models for Flow and Bed Topography in Channels With Periodic Width Variations

Source	Model	Boundary Conditions	Bed Load Formula	Incorporated Effects on Direction of Bed Load Motion
Bittner [1994]	2-D	no penetration of flow and sediment at the banks	Engelund-Hansen	secondary flow (depth-averaged velocity); local bed slope
Repetto et al. [2002]	2-D	no penetration of flow and sediment at the banks	*Parker* [1990]	secondary flow (depth-averaged velocity); local bed slope
	3-D	no slip at the bed; no penetration of flow and sediment at the banks; kinematic and dynamic conditions at the free surface	*Parker* [1990]	secondary flow (streamline curvature, convective acceleration); local bed slope
	2-D-k	no penetration of flow and sediment at the banks	*Parker* [1990]	secondary flow (streamline curvature, depth-averaged velocity); local bed slope
This study	2-D-C_s	no penetration of flow and sediment at the banks	Meyer-Peter and Müller	secondary flow (streamline curvature, depth-averaged velocity); local bed slope

displayed a spatial structure of side bars in the experiments of *Bittner* [1994] while according to the description of *Repetto et al.* [2002] either central or side bars may form, depending on the wave number of width variations. However, formation of different forced bars under their prescribed conditions has only been numerically demonstrated by *Repetto et al.* [2002] and thus remains to be verified experimentally. *Repetto et al.* [2002] claimed that generation of a central bar in a wide section pushes the thread of high velocity toward the banks, leading to an enhancement of width perturbation and thus a bifurcation of the channel. Accordingly, they used the longitudinal excess velocity at the banks calculated with three-dimensional (3-D) model as a criterion for predicting bank erosion (or planimetric instability). A drawback of this approach arises from the relaxed no-slip condition at the sidewalls, thus predictions of incipient bifurcation based on the distorted velocities in the near-bank region could lead to erroneous results especially for narrow channels in which the no-slip effect becomes significant.

[4] In this study we investigate the conditions under which different types of forced bars may form in channels with periodic width variations. A 2-D depth-averaged model of flow and bed topography is adopted for solving analytically the forced bed configuration. To accommodate the 3-D nature of the flow field, we use an approximate approach to incorporate the effect on transverse bed shear stress of the secondary helical flow induced by streamline curvature. An experimental study is conducted to provide a test of the model results. The forced bed forms are then classified into four types of bar pattern according to their geometric characteristics. The analytical solution is further used to establish the criteria for central bar formation, which implies a condition required for incipient bifurcation. The approach demonstrates the merit of using the resulting bed form as a criterion for predicting planimetric instability.

2. Previous Studies

[5] *Bittner* [1994] was perhaps the first to investigate theoretically and experimentally the equilibrium bed deformations induced by the forcing effect of width variations. In Bittner's work, a 2-D model was proposed and a linearized solution of flow and bed topography was obtained following the work of *Blondeaux and Seminara* [1985] and *Colombini et al.* [1987]. On the basis of Bittner's work, *Repetto et al.* [2002] also presented a 2-D model and a similar linear solution. The only difference between these two models is the formula used to predict bed load intensity. The Engelund-Hansen formula was used by *Bittner* [1994], but the bed load formula of *Parker* [1990] was employed by *Repetto et al.* [2002]. The effects of depth-averaged secondary flow and local bed slope on the direction of bed load motion were considered by both models (Table 1). However, these models did not account for the effect of helical flow induced by streamline curvature, thus were unable to predict any significant transverse bed deformation.

[6] To overcome this shortcoming, *Repetto et al.* [2002] developed a full 3-D model, in which the governing equations and boundary conditions were linearized into a sequence of ordinary differential equations, and a shooting procedure and fourth-order Runge-Kutta scheme was used to obtain a numerical solution. The helical flows induced by streamline curvature and convective acceleration were both accounted for in the 3-D model. *Repetto et al.* [2002] noticed that the novel feature associated with the 3-D model was the appearance of a transverse bed deformation, and went on to correct the 2-D model by incorporating the effect of helical flow. It was found that their corrected 2-D model could suitably describe the observed transverse variation of bed profile. In addition, the resulting phase shift and amplitude of flow and bed variables were comparable to those predicted by the 3-D model. However, the correction coefficient k in their modified 2-D model has relied on the 3-D solution. In this paper, we present an approximate approach that can be directly used to take into account the effect of local streamline curvature C_s on bed load motion without solving the 3-D problem (section 3.1.2). Hereinafter the corrected 2-D models of *Repetto et al.* [2002] and the authors are referred to as 2-D-k and 2-D-C_s models, respectively. A summary of the models discussed here is provided in Table 1.

3. Theory

[7] The formulation of the problem and the linearized solution (sections 3.1.1 and 3.2) follow closely the work of *Bittner* [1994] and *Repetto et al.* [2002], while in section 3.1.2 we present an approximate approach to account for the helical flow effect induced by streamline curvature.

3.1. Depth-Averaged Two-Dimensional Model

3.1.1. Formulation of Problem

[8] Consider a straight channel with average width $2B_0^*$ over which periodic variations are superimposed (Figure 1). The sidewalls of the channel are described by

$$y^* = \pm b^* = \pm B_0^*[1 + A\cos(\lambda_p^* x^*)], \quad (1)$$

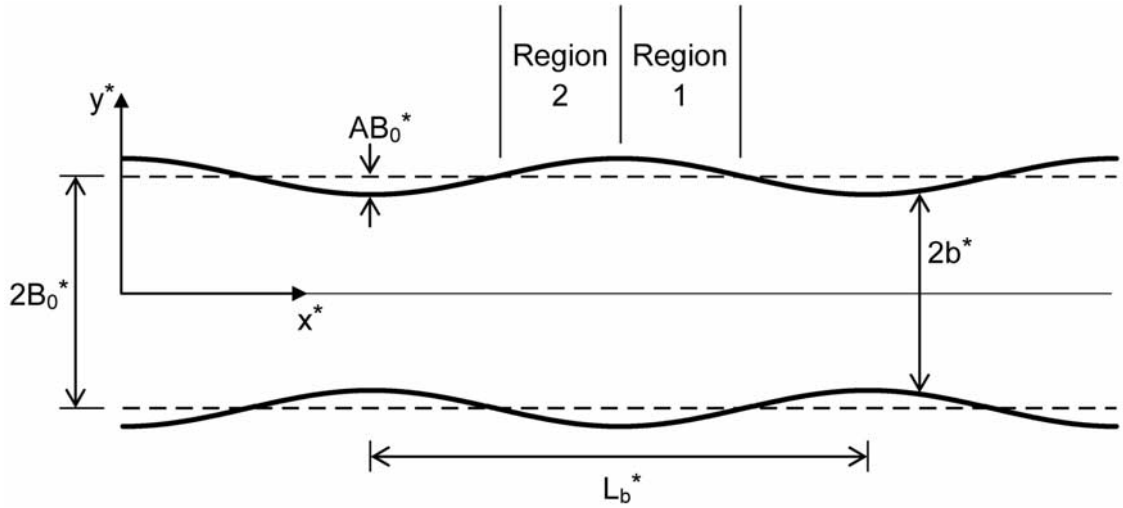

Figure 1. Definition sketch of channel geometry and notations. Regions 1 and 2 are the areas in the channel covering a 1/4 wavelength immediately downstream and upstream of the widest sections, respectively.

where x^* and y^* are the longitudinal and transverse coordinates (hereinafter the superscript asterisks denote dimensional variables), b^* is the local half-width of the channel, A is a dimensionless small amplitude of width variations, λ_b^* is the wave number of width variations defined by $2\pi/L_b^*$, in which L_b^* is the wavelength of width variations. The physical domain is stretched into a rectangle by normalizing the transverse coordinate y^* with the local width b^*, i.e.,

$$y = y^*/b^*(x^*), \tag{2}$$

so that y ranges from -1 to 1. Furthermore, the following dimensionless variables are defined:

$$(x, b) = (x^*, b^*)/B_0^*, \tag{3a}$$

$$(U, V) = (U^*, V^*)/U_0^*, \tag{3b}$$

$$(H, D) = (H^*, D^*)/D_0^*, \tag{3c}$$

$$\lambda_b = \lambda_b^* B_0^*, \tag{3d}$$

$$(\tau_x, \tau_y) = (\tau_x^*, \tau_y^*)/\rho U_0^{*2}, \tag{3e}$$

$$(q_x, q_y) = (q_x^*, q_y^*)/d_s^* \sqrt{Rgd_s^*}, \tag{3f}$$

where (U^*, V^*) is the velocity vector; H^* and D^* are water level and depth, respectively; U_0^* and D_0^* are average velocity and depth of a reference uniform flow in the channel with constant width $2B_0^*$, for given water discharge, slope, and grain size; (τ_x^*, τ_y^*) is the bed shear stress vector; (q_x^*, q_y^*) is the sediment transport vector per unit width; d_s^* is the sediment diameter; $R = (\rho_s - \rho)/\rho$, where ρ_s and ρ are sediment and water densities, respectively; g is the gravitational acceleration.

[9] To look for the steady configuration induced by width variations, time derivatives are neglected in the depth-averaged 2-D flow equations (i.e., continuity equation, longitudinal and transverse momentum equations) and sediment continuity equation. With equations (2) and (3), flow and sediment equations take the following dimensionless form:

$$b\frac{\partial(UD)}{\partial x} + \frac{\partial(VD)}{\partial y} - y\frac{\partial b}{\partial x}\frac{\partial(UD)}{\partial y} = 0, \tag{4a}$$

$$bU\frac{\partial U}{\partial x} + V\frac{\partial U}{\partial y} + \frac{b}{F_0^2}\frac{\partial H}{\partial x} + b\frac{\beta\tau_x}{D} - y\frac{\partial b}{\partial x}U\frac{\partial U}{\partial y} - \frac{y}{F_0^2}\frac{\partial b}{\partial x}\frac{\partial H}{\partial y} = 0, \tag{4b}$$

$$bU\frac{\partial V}{\partial x} + V\frac{\partial V}{\partial y} + \frac{1}{F_0^2}\frac{\partial H}{\partial y} + b\frac{\beta\tau_y}{D} - y\frac{\partial b}{\partial x}U\frac{\partial V}{\partial y} = 0, \tag{4c}$$

$$b\frac{\partial q_x}{\partial x} + \frac{\partial q_y}{\partial y} - y\frac{\partial b}{\partial x}\frac{\partial q_x}{\partial y} = 0, \tag{4d}$$

where β is the average aspect (or width to depth) ratio, defined by B_0^*/D_0^*; F_0 is the Froude number of the reference uniform flow, defined as $U_0^*/\sqrt{gD_0^*}$. Boundary conditions are given to impose no penetration of fluid and sediment at the banks, which can be expressed in the dimensionless form as follows:

$$-U\frac{\partial b}{\partial x} \pm V = 0 \quad \text{at } y = \pm 1 \tag{5a}$$

$$-q_x\frac{\partial b}{\partial x} \pm q_y = 0 \quad \text{at } y = \pm 1. \tag{5b}$$

The effect of width variations is felt through the dependence on the shape of the banks embodied in the term $\partial b/\partial x$. It is emphasized here that the no-slip condition should be also

imposed on the sidewalls. However, considering both no-penetration and no-slip conditions could result in much more complication as no appropriate distributions of the variables could be assigned to satisfy both conditions, especially for the drastic spatial variation near the sidewalls due to the no-slip condition. Here we follow the work of *Bittner* [1994] and *Repetto et al.* [2002] by relaxing the no-slip boundary condition. Such a simplified treatment is acceptable for studying the bed topography of natural channels featuring large width ratios in which the no-slip effect becomes negligible. However, considerable errors may arise in the near-bank region especially for narrow channels (see sections 5.1.1 and 6.2).

3.1.2. Correction for Effect of Secondary Helical Flow

[10] The governing equations and boundary conditions given above are, however, insufficient to describe the flow and bed topography developing in a channel with periodic width variations. Many previous studies indicated that channel curvature, which would give rise to the secondary helical flow, has major impacts on redistribution of the primary flow and bed topography [e.g., *Leschziner and Rodi*, 1979; *Kalkwijk and de Vriend*, 1980; *de Vriend*, 1981; *Kitanidis and Kennedy*, 1984; *Johannesson and Parker*, 1989a, 1989b]. In straight channels with variable width, although the main axis is nonsinuous, minor streamline distortion is perceptible from one section to another. As a result, the secondary helical flows will be induced by the streamline curvature and make contributions to the transverse bed deformation. Numerical results of the 3-D model [*Repetto et al.*, 2002] have clearly demonstrated the existence of such helical flows.

[11] In this study a depth-averaged 2-D model is adopted, thus it is unlikely to acquire a 3-D picture of the flow field including the secondary helical flow. However, since we are mainly interested in the final bed configuration, the effect of streamline curvature is incorporated into the bed shear stress, which would then affect sediment transport and thus bed topography. Using this approach, we take advantage of the 2-D model allowing a closed-form solution of flow and bed topography while still retaining sufficient accuracy, especially for bed topography. A previous correction scheme for the effect of helical flow was presented by *Repetto et al.* [2002]. However, their correction coefficient k, a complex parameter accounting for the possibility of a phase lag between helical flow and bank profile, is determined from the helical flow distribution obtained through their 3-D model. Though it may provide a more accurate correction, the dependence upon the asymptotic 3-D numerical solution violates our intension to seek an analytical solution of bed deformation that can be directly used to determine the criteria for incipient bifurcation. Moreover, we will demonstrate in section 5.1 the utility of our approach by showing that our 2-D-C_s model gives satisfactory results comparable to those of a 3-D model.

[12] Here we use an approximate approach to account for the effect of streamline curvature on transverse bed shear stress. Recall that, to analyze the effect of secondary flow on bed load motion, *Blondeaux and Seminara* [1985] introduced an angle χ to describe the difference between the local direction of bed shear stress and x^* direction. The angle χ was expressed as a function of two different terms representing the contributions due to the depth-averaged flow and the zero-average helical flow driven by channel curvature, respectively. Herein we replace the effect of channel curvature included in the second term by the effect of streamline curvature, and revise the expression for χ as follows:

$$\sin\chi = \frac{V}{(U^2+V^2)^{1/2}} - a\frac{D}{\beta}C_s, \tag{6}$$

where a is a constant ranging between 7 and 12 in curved channels [*Engelund*, 1974], which is taken to be 17 in this study, leading to satisfactory agreement with experimental data (see section 5.1.1); C_s is the dimensionless local curvature of streamline [*Repetto et al.*, 2002], defined by

$$C_s = \frac{-\partial(V/U)/\partial x}{\left[1+(V/U)^2\right]^{3/2}}. \tag{7}$$

Note that in equation (6) we assume that the correction is in phase with streamline curvature (i.e., the coefficient a is a real parameter), thus the possible phase lag is not accounted for in our 2-D-C_s model. However, as will be shown in section 5.1.2, the results obtained from the 2-D-C_s model are comparable to those obtained from the 2-D-k model, indicating that such a phase lag may not be very significant. *Blondeaux and Seminara* [1985] further employed an expression that relates bed shear stress components with a friction coefficient C_f, i.e.,

$$(\tau_x,\tau_y) = (U,V)\left(U^2+V^2\right)^{1/2}C_f, \tag{8}$$

where

$$C_f^{-1/2} = 6 + 2.5\ln(D/2.5d_s) \tag{9a}$$

$$d_s = d_s^*/D_*^*. \tag{9b}$$

In the presence of secondary helical flows, the transverse velocity V in equation (8) is revised with equation (6), so that the transverse component of bed shear stress is corrected, which is expressed by

$$(\tau_x,\tau_y) = (U,V_s)\left(U^2+V^2\right)^{1/2}C_f, \tag{10}$$

where

$$V_s = V - aDC_s\left(U^2+V^2\right)^{1/2}/\beta. \tag{11}$$

Since the helical flow is zero-average over a cross section, V_s only appears in the transverse bed shear stress τ_y, but not in the average velocity $(U^2+V^2)^{1/2}$.

3.1.3. Closure Relations

[13] The direction of bed load motion is affected not only by the secondary flow (angle χ), but also by the local bed slope, which is described by *Blondeaux and Seminara* [1985] as follows:

$$\sin\alpha = \sin\chi - \frac{r}{\beta\sqrt{\theta}}\frac{\partial\eta}{\partial y}, \tag{12}$$

where α denotes the angle between average particle path and x^* axis; $\eta = H - D$ is the dimensionless bed level; r is an empirical coefficient ranging between 0.3 and 1 [*Ikeda*, 1982; *Talmon et al.*, 1995], a value of 0.3 is used herein accounting for the gently varying transverse bed gradient; θ is the local value of dimensionless bed shear stress (Shields stress), defined by

$$\theta = \tau^*/(\rho_s - \rho)g d_s^*, \tag{13}$$

where $\tau^* = \sqrt{\tau_x^{*2} + \tau_y^{*2}}$, in which (τ_x^*, τ_y^*) are converted from the values of (τ_x, τ_y) obtained from equation (10). The bed load components are evaluated with a well-established relation [e.g., *Ikeda*, 1982; *Blondeaux and Seminara*, 1985; *Talmon et al.*, 1995], given by

$$(q_x, q_y) = (\cos\alpha, \sin\alpha)\Phi, \tag{14}$$

where Φ is the bed load intensity, determined from the Meyer-Peter and Müller formula [*Chien*, 1956]:

$$\Phi = 8(\theta - \theta_c)^{3/2}, \tag{15}$$

where θ_c is the dimensionless critical shear stress, for well-sorted sediment θ_c was found to be $\sim$0.04 [e.g., *Wilcock*, 1998; *Wu and Chou*, 2003]. With equations (10) and (14), the unknowns in (4) are reduced to (U, V, H, D), hence the system of equations is ready to be solved.

3.2. Linear Solution

[14] The perturbation method is employed in search of the analytical solution to the problem. The essential idea of this method is to obtain an asymptotic solution by expanding the variables in question using a small perturbation δ. A variable is broken into an unperturbed mean value and a perturbed term, such that (b, U, V, H, D, η) can be expressed as

$$(b, U, V, H, D, \eta) = (1, 1, 0, H_0, 1, H_0 - 1) + (b', U', V', H', D', \eta'), \tag{16}$$

where $H_0 = H_0^*/D^*_0$, and H_0^* is the local mean water level corresponding to the reference uniform flow; (b', U', V', H', D', η') are the perturbed terms. Since the channel width exhibits a periodic variation, as described by (1), the perturbed terms can be expanded as

$$(b', U', V', H', D', \eta') = \delta[(1, U_1, V_1, H_1, D_1, \eta_1)\exp(i\lambda_b x) + \text{c.c.}] + O(\delta^2), \tag{17}$$

where $\delta = A/2$, with A already defined in equation (1); (U_1, V_1, H_1, D_1, η_1) are complex numbers varying with y only; $\exp(i\lambda_b x) = \cos(\lambda_b x) + i\sin(\lambda_b x)$; c.c. denotes complex conjugates. Equation (17) is based on the assumption that the variation frequencies of the perturbed terms are identical to that of width variations (but not necessarily in phase). The assumption of small-amplitude width variations (i.e., $\delta \ll 1$) allows us to neglect the higher-order terms $O(\delta^2)$, the linear solution to the problem thus reads

$$(U, V, H, D) = (1, 0, H_0, 1) + \delta[(U_1, V_1, H_1, D_1)\exp(i\lambda_b x) + \text{c.c.}]. \tag{18}$$

Introducing equation (18) into (10) and (14), and then substituting the resulting expressions for (τ_x, τ_y) and (q_x, q_y) along with equation (18) into (4a)–(4d), gives a zeroth-order and a first-order systems of equations.

[15] At $O(\delta^0)$, the solution for the reference uniform flow is recovered, i.e.,

$$\frac{dH_0}{dx} = -\beta C_{f0} \tag{19a}$$

$$q_{x0} = \Phi_0 = 8(\theta_0 - \theta_c)^{3/2}, \tag{19b}$$

where $C_{f0} = [6 + 2.5\ln(1/2.5d_s)]^{-2}$ is the friction coefficient of the unperturbed reference uniform flow; $\theta_0 = \tau_0^*/(\rho_s - \rho)g d_s^*$, in which τ_0^* is the bed shear stress corresponding to the reference uniform flow. At $O(\delta)$, the following system of equations is obtained:

$$a_1 U_1 + \frac{dV_1}{dy} + a_1 D_1 = 0, \tag{20a}$$

$$a_2 U_1 + a_3 H_1 + a_4 D_1 = 0, \tag{20b}$$

$$a_5 V_1 + a_6 \frac{dH_1}{dy} = 0, \tag{20c}$$

$$a_7 U_1 + a_8 \frac{dV_1}{dy} + a_9 \frac{d^2(H_1 - D_1)}{dy^2} + a_{10} D_1 = 0, \tag{20d}$$

where the coefficients $a_1 \sim a_{10}$ are defined by

$$a_1 = i\lambda_b, \quad a_2 = i\lambda_b + 2\beta C_{f0}, \quad a_3 = i\lambda_b F_0^{-2}, \quad a_4 = \beta C_{f0}(s_1 - 1),$$
$$a_5 = i\lambda_b + \beta C_{f0}(1 + ai\lambda_b/\beta), \quad a_6 = F_0^{-2}, \quad a_7 = i\lambda_b s_2,$$
$$a_8 = 1 + ai\lambda_b/\beta, \quad a_9 = -r/\beta\sqrt{\theta_0}, \quad a_{10} = i\lambda_b s_3$$

and

$$s_1 = \frac{1}{C_{f0}}\left(\frac{dC_f}{dD}\right)_{D=1}, \quad s_2 = \frac{2\theta_0}{\Phi_0}\left(\frac{d\Phi}{d\theta}\right)_{\theta=\theta_0}, \quad s_3 = s_1 s_2/2.$$

The linearized form of the boundary conditions (5a)–(5b) is given by

$$V_1 = \pm i\lambda_b \quad \text{at } y = \pm 1 \tag{21a}$$

$$\frac{d(H_1 - D_1)}{dy} = \mp\frac{a\sqrt{\theta_0}}{r}\lambda_b^2 \quad \text{at } y = \pm 1. \tag{21b}$$

Note that equation (21b), which is different from equation (2.16b) in the work of *Repetto et al.* [2002] due to the correction made in (6), indicates that the transverse bed slopes at the sidewalls are nonzero values. Equations (20a)–(20d) and the linearized boundary conditions (21a)–(21b) can be further simplified as a fourth-order ordinary system for the variable V_1:

$$\Gamma_0 \frac{d^4 V_1}{dy^4} + \Gamma_1 \frac{d^2 V_1}{dy^2} + \Gamma_2 V_1 = 0, \tag{22a}$$

$$V_1 = \pm i\lambda_b \quad \text{at } y = \pm 1, \tag{22b}$$

$$\frac{d^2 V_1}{dy^2} = \pm \Gamma_3 \quad \text{at } y = \pm 1, \tag{22c}$$

where

$$\Gamma_0 = a_2 a_9 / a_1 (a_2 - a_4),$$
$$\Gamma_1 = a_8 - \frac{a_7}{a_1} + \frac{a_2(a_{10} - a_7)}{a_1(a_4 - a_2)} + \frac{a_5 a_9 (a_2 - a_3 - a_4)}{a_6(a_4 - a_2)},$$
$$\Gamma_2 = a_3 a_5 (a_{10} - a_7) / a_6 (a_4 - a_2),$$
$$\Gamma_3 = \frac{a_1(a_4 - a_2)}{a_2}\left(\frac{a\lambda_b^2\sqrt{\theta_0}}{r}\right) + \frac{a_1^2 a_5 (a_2 - a_3 - a_4)}{a_2 a_6}.$$

The analytical solution to the problem defined by (22) can be readily obtained, i.e.,

$$V_1 = \gamma_1 \sinh(\lambda_1 y) + \gamma_2 \sinh(\lambda_2 y), \tag{23}$$

where

$$\lambda_1 = \sqrt{\frac{1}{2}\left[-\frac{\Gamma_1}{\Gamma_0} + \sqrt{\left(\frac{\Gamma_1}{\Gamma_0}\right)^2 - 4\left(\frac{\Gamma_2}{\Gamma_0}\right)}\right]},$$
$$\lambda_2 = \sqrt{\frac{1}{2}\left[-\frac{\Gamma_1}{\Gamma_0} - \sqrt{\left(\frac{\Gamma_1}{\Gamma_0}\right)^2 - 4\left(\frac{\Gamma_2}{\Gamma_0}\right)}\right]}$$

and

$$\gamma_1 = \frac{\Gamma_3 - i\lambda_b \lambda_2^2}{(\lambda_1^2 - \lambda_2^2)\sinh(\lambda_1)}, \quad \gamma_2 = \frac{\Gamma_3 - i\lambda_b \lambda_1^2}{(\lambda_2^2 - \lambda_1^2)\sinh(\lambda_2)}.$$

Substituting equation (23) into (20a)–(20c), we obtain the rest of the variables:

$$U_1 = \gamma_3 \cosh(\lambda_1 y) + \gamma_4 \cosh(\lambda_2 y), \tag{24a}$$

$$H_1 = \gamma_5 \cosh(\lambda_1 y) + \gamma_6 \cosh(\lambda_2 y), \tag{24b}$$

$$D_1 = \gamma_7 \cosh(\lambda_1 y) + \gamma_8 \cosh(\lambda_2 y), \tag{24c}$$

where

$$\gamma_3 = \frac{1}{a_4 - a_2}\left(a_3\gamma_5 + \frac{a_4}{a_1}\lambda_1\gamma_1\right),$$
$$\gamma_4 = \frac{1}{a_4 - a_2}\left(a_3\gamma_6 + \frac{a_4}{a_1}\lambda_2\gamma_2\right),$$
$$\gamma_5 = -\frac{a_5\gamma_1}{a_6\lambda_1}, \quad \gamma_6 = -\frac{a_5\gamma_2}{a_6\lambda_2},$$
$$\gamma_7 = \frac{1}{a_4 - a_2}\left(\frac{a_2}{a_1}\lambda_1\gamma_1 - a_3\gamma_5\right),$$
$$\gamma_8 = \frac{1}{a_4 - a_2}\left(\frac{a_2}{a_1}\lambda_2\gamma_2 - a_3\gamma_6\right).$$

Once H_1 and D_1 are solved, η_1 can be directly determined by $H_1 - D_1$.

4. Experiments

[16] The experimental study was conducted in a slope-adjustable recirculating flume, 40 cm in width and 12 m in length, located at the Hydrotech Research Institute, NTU. The flow rate was controlled electronically and the water depth was adjusted using a tailgate at the end of the flume. An acrylic channel with sinusoidally varying width was placed inside the flume (Figure 2). The average width of the channel, $2B_0^*$, was 32 cm; the amplitude of width variations, AB_0^*, was 2.5 cm, leading to a value of $\delta = 0.078$; the wavelength of width variations, L_0^*, was 335 cm, which corresponds to a value of $\lambda_b = 0.3$, where $\lambda_b = \lambda_0^* B_0^*$ is the dimensionless wave number. The wide and narrow sections were 37 cm and 27 cm in width, respectively; the void space between the channel and flume was sealed to ensure that all the flow would enter the channel. The length of the channel was 10 m, consisting of three full cycles of width variations. Upstream of the channel was a series of energy dissipation and flow regulating devices; immediately downstream of the channel was a bed load trap installed on the bottom of the flume. The sediment used in this study was well-sorted sand, with $d_s^* = 1.58$ mm and $\rho_s/\rho = 2.63$.

[17] Bed topography was measured using a DTM scanning system, which included a digital camera and a laser sheet projector both mounted on an electric carriage moving along the rails (Figure 2). At the beginning of each run, a calibration procedure was performed and a projective matrix was constructed to establish the relationship between the 2-D images taken by the camera and the corresponding 3-D coordinates (see *Spinewine et al.* [2003] for details). After each run, the carriage traveled along the flume and the laser sheet projected on the bed formed a distorted line due to bed deformation (Figure 3). The camera photographed the distorted line at an equal time (thus distance) interval. The DTM data were then obtained by converting each distorted line into 3-D coordinates at the specified grids through the established projective matrix. Bed topography of the two sinusoidal cycles in the middle was scanned, where no significant entrance or backwater effect was observed.

[18] The bottom of the channel was paved with a 10-cm-thick sand bed. At the beginning of each experiment, the sand bed was flattened, and the flume slope was adjusted to a specified value. The initial bed configuration was recorded with the DTM scanning system. A small flow was then

Figure 2. Photograph showing the experimental setup and DTM scanning system. Shown in the front is the laser sheet projected on the bed and the resulting distorted laser line.

supplied to the flume and the tailgate was raised to store water in the channel, with special care taken to ensure that minimal disturbances would be exerted on the bed. Once the water was raised to a certain level, the flow rate was gradually increased while the tailgate was gradually lowered until a prescribed quasi-uniform flow was achieved. The depths of water were measured at eight locations uniformly distributed over two sinusoidal cycles, the average of which was taken to be the depth of reference uniform flow, D_0^*. During each run, the sediment collected at the bed load trap was returned to upstream every 15 to 30 minutes, depending on the transport rate. The flow kept running until a steady state was reached, which was confirmed by the observed steady bed forms and equilibrium bed load transport. Usually 8 to 12 hours were needed to reach this steady state, after which the flow was switched off and the water was slowly drained. The final bed configuration was then scanned. The difference between the final and initial bed elevations gave the bed level perturbation η'^*. A total of 15 runs were performed with various conditions (see Table 2), covering the ranges of $3.6 \leq \beta \leq 13.5$, $0.045 \leq \theta_0 \leq 0.103$, and $0.035 \leq d_s \leq 0.133$, where $\tau_0^* = \gamma D_0^* S$ was used to calculate θ_0, in which γ is the specific weight of water, and S is the channel slope. These ranges are comparable to those used by *Repetto et al.* [2002]. Formation of alternate bars was very sensitive to disturbances that might appear at the entrance. For the 15 runs, 6 were categorized as stable runs in which only forced bars were present (S series), while the remaining 9 runs were associated with migrating or stationary alternate bars (F series). Shown in Figures 4a and 4b are the central bar observed in run S-6 and the alternate bars observed in run F-1, respectively. Because experiments of forced bars under stable regimes require special efforts and are relatively rare, the bed deformation data discussed here are made available as auxiliary material[1].

5. Results

5.1. Comparison of Model Results

[19] In section 5.1.1 we compare the experimental results with the predicted results of our 2-D-C_s model that includes the helical flow effect induced by streamline curvature and two 2-D models that neglect the helical flows; while in section 5.1.2 we compare the results of our 2-D-C_s model with those of the 3-D and 2-D-k models presented by *Repetto et al.* [2002], all incorporating the effect of helical flow.

5.1.1. Comparison With Models Neglecting Helical Flow Effect

[20] A typical forced bed form (central bar) observed in run S-6 is shown in Figure 5 along with the results predicted by our 2-D-C_s model (incorporating the helical flow effect) and two previous 2-D models (neglecting the helical flow effect) of *Bittner* [1994] and *Repetto et al.* [2002]. The experimental result (Figure 5a) demonstrates a longitudinal trend of deposition at the wide sections and scour at the narrow ones, with the magnitudes of maximum deposit and scour both on the order of 1 cm. The bed form predicted by the 2-D-C_s model (Figure 5b) is in satisfactory agreement with the observed result. The previous 2-D models are, however, unable to reproduce the transverse bed deformation without including the effect of helical flow; only the longitudinal component is captured (Figures 5c and 5d). These are further demonstrated by the longitudinal and transverse profiles of bed deformation (Figures 6 and 7). Figure 6a shows that similar longitudinal profiles of bed deformation (along the centerline) are obtained by different models, which coincide well with the experimental result. The transverse profiles of bed deformation shown in Figure 7 demonstrate that the results of the previous 2-D models lack any significant transverse variation. *Repetto et al.* [2002] reached a similar conclusion by comparing the results of their 2-D and 3-D models. The transverse profiles of bed deformation predicted by the 2-D-C_s model are in good agreement with the experimental data. At the narrow sections, however, the 2-D-C_s model tends to underestimate the scour depth at the center although the general trend of concave profile is captured. Such a discrepancy arises from the relaxed no-slip condition at the sidewalls, as previously

[1] Auxiliary material is available at ftp://ftp.agu.org/apend/jf/2004JF000160.

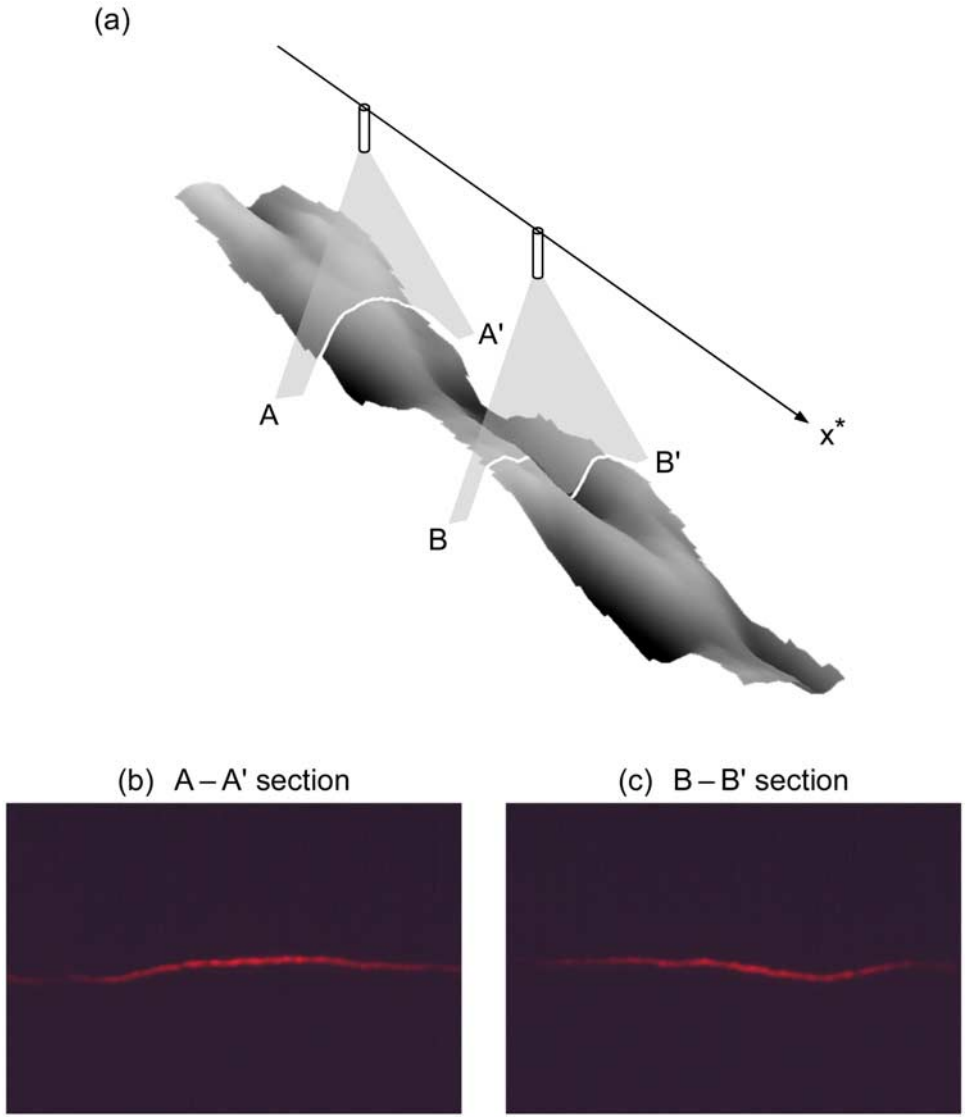

Figure 3. Illustration of (a) laser sheets projected on the bed and digital images of distorted laser lines taken at (b) A-A′ and (c) B-B′ sections.

mentioned in section 3.1.1 and will be discussed later in this section.

[21] To further test the models on different types of bed form, the forced bars observed in the flume experiments of *Bittner* [1994] were also used. The experimental data of *Bittner* [1994] include 23 runs (β ranging from 7.9 to 12.2) performed in two channels ($\delta = 0.38$ and 0.15 in channels 1 and 2, respectively), among which 11 runs were stable and associated with symmetric forced bars. A typical forced bed form (side bars) observed in run C1-11 ($\lambda_b = 0.8$, $S = 0.004$, $\beta = 9.1$, $d_s = 0.024$, $\theta_0 = 0.102$) is shown in Figure 8 along with the predictions of different models. The experimental result (Figure 8a) demonstrates a consistent longitudinal trend of bed deformation, only now the maximum deposition occurred at both sides of the wide section. The flow intensity through the constriction was sufficiently high such that the deposit at the wide section was cut through at the center leading to two separate bars at the sides and a downstream central deposit. This qualitative feature is captured by the 2-D-C_s model (Figure 8b). The 2-D model of *Bittner* [1994] fails to replicate the bed form of side bars, but demonstrates a purely central bar at the wide section (Figure 8c). The 2-D model of *Repetto et al.* [2002] appears to capture the transverse bed deformation (Figure 8d), although weak and slightly out of phase with the observed result.

[22] The amplitudes and shapes of these forced bars are further demonstrated by the longitudinal and transverse profiles of bed deformation (Figures 6 and 9). Figure 6b shows the longitudinal profiles of bed deformation (along the centerline) obtained by three different models. Overall, the longitudinal profile predicted by the 2-D-C_s model is in reasonably good agreement with the experimental data; minor discrepancies arise from eliminating the nonlinear perturbation terms in the analytical solution whose effect becomes less negligible for a larger value of δ (= 0.38) [*Wu and Yeh*, 2004]. The longitudinal profile of bed deformation predicted by the 2-D model of *Repetto et al.* [2002] is similar to that obtained by the 2-D-C_s model, but exhibits a phase lag with respect to the observed result. Such a phase

Table 2. Summary of Experimental Conditions and Observed Bed Forms[a]

Run[b]	S	D_0^*, cm	U_0^*, m/s	θ_0	β	d_s	Observed Bar Type[c]
F-1	0.005	2.31	0.351	0.045	6.9	0.068	A, N
F-2	0.005	3.13	0.438	0.061	5.1	0.050	B, C
F-3	0.005	3.65	0.489	0.071	4.4	0.043	B, C
F-4	0.007	3.03	0.506	0.082	5.3	0.052	B, C
F-5	0.007	1.91	0.361	0.052	8.4	0.083	B, N
F-6	0.007	1.89	0.357	0.051	8.5	0.084	B, S
F-7	0.01	1.19	0.298	0.046	13.5	0.133	A, S
F-8	0.01	2.64	0.547	0.103	6.1	0.060	B, C
F-9	0.005	2.96	0.420	0.057	5.4	0.053	B, N
S-1	0.004	3.31	0.408	0.052	4.8	0.048	C
S-2	0.004	4.40	0.500	0.068	3.6	0.036	C
S-3	0.005	2.91	0.416	0.057	5.5	0.054	C
S-4	0.005	3.24	0.449	0.063	4.9	0.049	C
S-5	0.003	4.06	0.409	0.047	3.9	0.039	C
S-6	0.003	4.49	0.439	0.052	3.6	0.035	C

[a]Abbreviations are as follows: S, channel slope; D_0^*, depth of reference uniform flow; U_0^*, velocity of reference uniform flow; θ_0, Shields stress of reference uniform flow; β, aspect ratio; d_s, dimensionless size.

[b]F series includes the unstable runs in which alternate bars and forced bed forms coexisted; S series includes the stable runs in which only forced bars were present.

[c]A, migrating alternate bars; B, stationary alternate bars; S, side bars; C, central bars; N, forced bed form not identified.

lag was already demonstrated numerically by *Repetto et al.* [2002]. The amplitude of longitudinal bed deformation predicted by the 2-D model of *Bittner* [1994] is least accurate among the three, with the maximum deposition nearly twice greater than those predicted by the other two. Since the only difference between the two previous 2-D models is the bed load formula adopted (see Table 1), the disagreement between their results is believed to originate from this.

[23] Figure 9a shows that the 2-D-C_s model suitably replicates the transverse bed deformation at the wide section, with the near-bank deposition slightly overestimated. The transverse variation predicted by the 2-D model of *Repetto et al.* [2002] is weak, while the transverse profiles predicted by the 2-D model of *Bittner* [1994] are totally out of phase with the observed results (Figures 9a and 9b). Moreover, Figure 9b shows that the 2-D-C_s model tends to overestimate the scour depth near the bank but underestimate that near the center of a narrow section, which is attributable to the neglected no-slip boundary condition whose effect becomes significant at the narrow sections. The no-slip condition would retard the flow near the bank and concentrate it toward the center, which would result in a decrease of bed shear stress near the bank but an increase near the center. Taking into account the no-slip boundary condition would thus lead to a decrease of scour depth near the bank and an increase near the center, such that the discrepancies demonstrated in Figure 9b could be reduced.

[24] A comparison of the observed amplitudes of forced bars with those predicted by the 2-D-C_s model is shown in Figure 10, where the maximum bar heights H_{BM}^*, defined as the difference between the highest and lowest bed levels within a bar wavelength, are demonstrated. The results

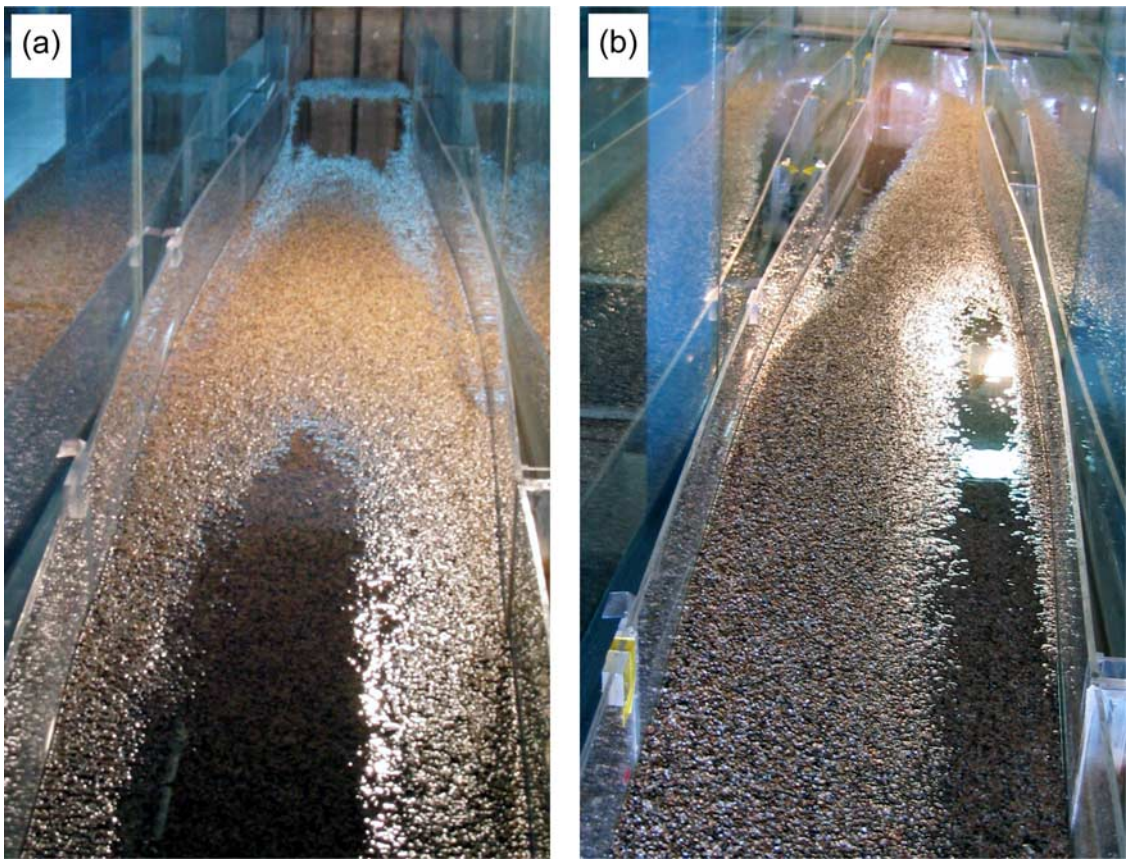

Figure 4. Photographs showing (a) central bar observed in run S-6 and (b) alternate bars observed in run F-1.

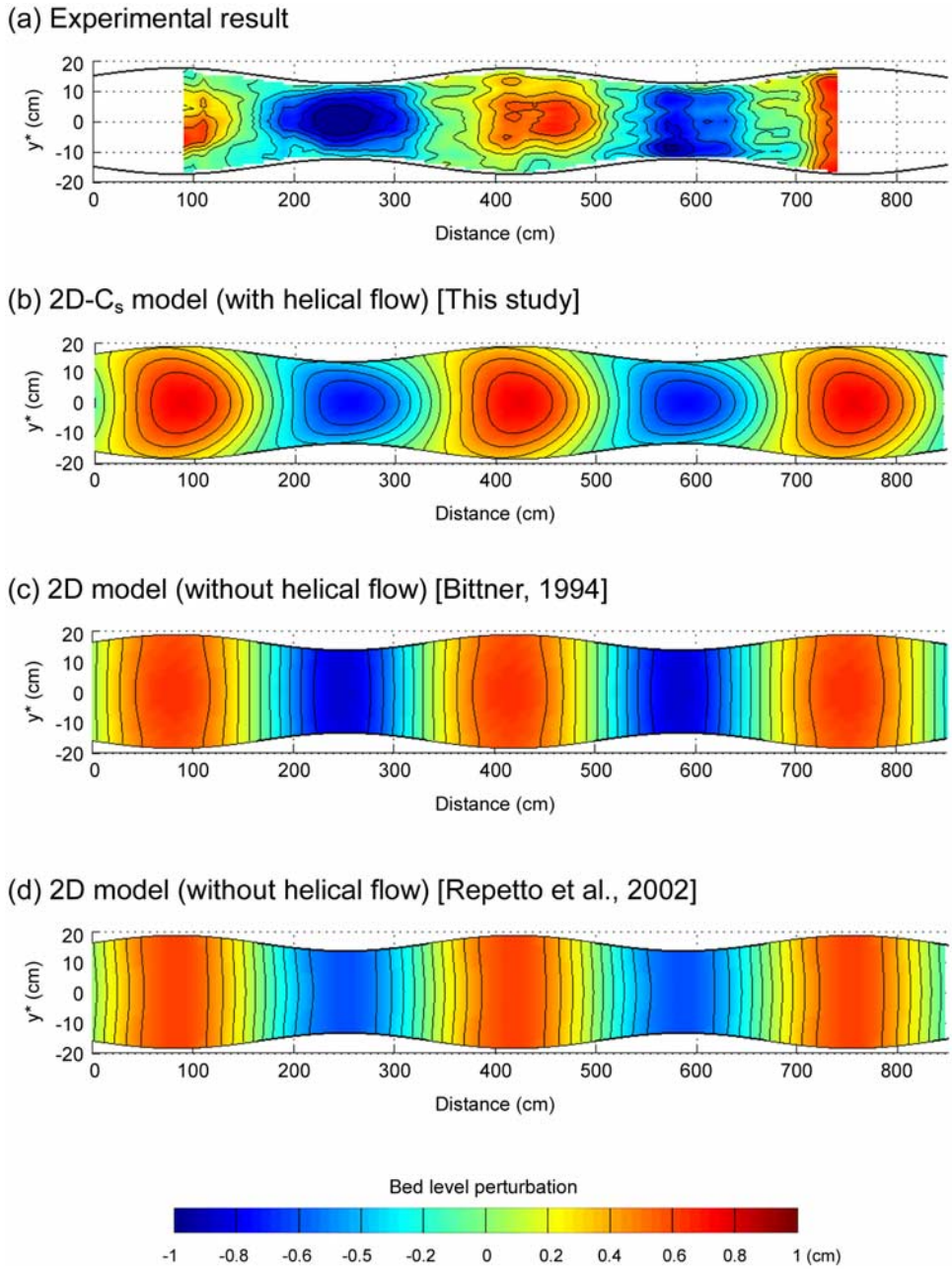

Figure 5. Contour plots showing (a) forced bars observed in run S-6 and predicted results of (b) 2-D-C_s model (this study), (c) 2-D model [*Bittner*, 1994], and (d) 2-D model [*Repetto et al.*, 2002] ($\lambda_b = 0.3$, $\theta_0 = 0.052$, $d_s = 0.035$, $\beta = 3.6$).

indicate that the 2-D-C_s model tends to overestimate the maximum bar heights of side bars but underestimate those of central bars. It has been speculated by *Bittner* [1994] that the linearized solution may not be valid for the large values of δ used in their experiments. In addition, the neglected no-slip condition discussed above may play a role in yielding such errors. Nevertheless, since we take our main interest in the development of different bed forms rather than the precise evaluation of their amplitudes (see section 6.2), the 2-D-C_s model may well serve as an useful tool for predicting bar patterns as long as it produces results comparable to those obtained by the 3-D or 2-D-k model, which will be discussed subsequently in more detail.

5.1.2. Comparison With Models Incorporating Helical Flow Effect

[25] To compare the models that incorporate the effect of helical flow, the results obtained from the 3-D and 2-D-k models of *Repetto et al.* [2002] and our 2-D-C_s model are shown in Figure 11, where the transverse profiles of bed deformation at different values of x (i.e., different sections) are demonstrated ($\theta_0 = 0.1$, $d_s = 0.05$, and $\beta = 10$). For the smaller wave number ($\lambda_b = 0.3$), the models predict formation of central bars at the wide sections ($x = 0$). As the wave

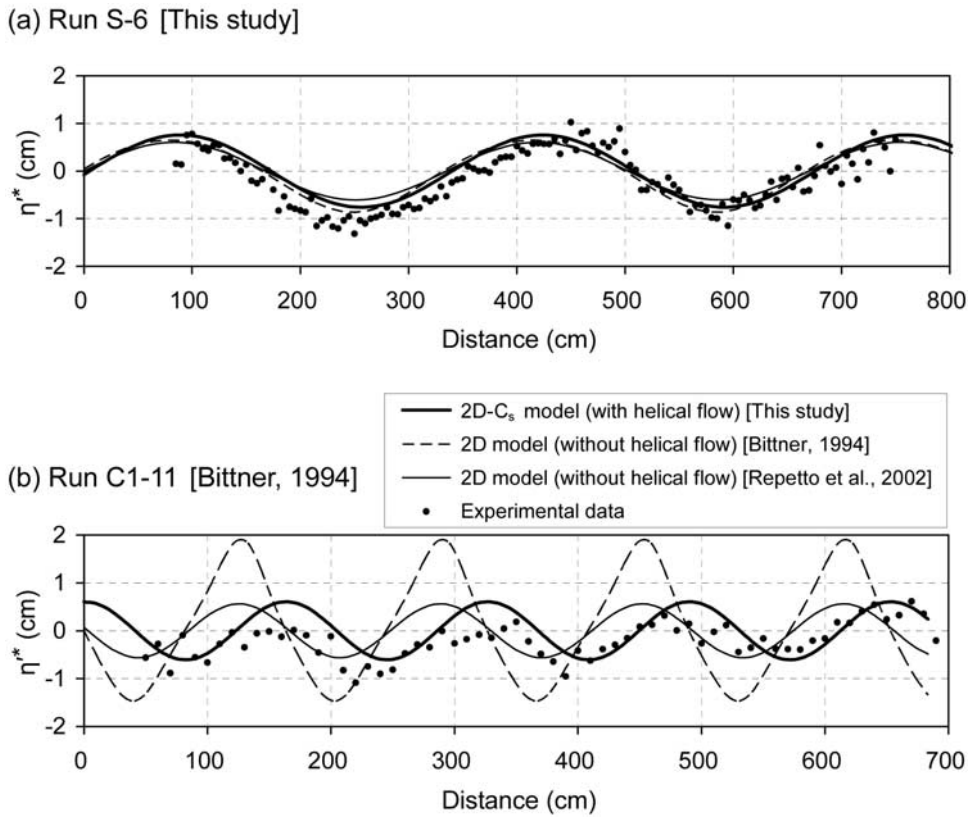

Figure 6. Longitudinal profiles of observed and predicted bed deformations at the centerline. (a) Run S-6 (this study) ($\lambda_b = 0.3$, $\theta_0 = 0.052$, $d_s = 0.035$, $\beta = 3.6$). (b) Run C1-11 [*Bittner*, 1994] ($\lambda_b = 0.8$, $\theta_0 = 0.102$, $d_s = 0.024$, $\beta = 9.1$).

number increases ($\lambda_b = 0.5$), the central bars would shift downstream leading to a pattern of side bars at the wide sections [*Repetto et al.*, 2002]. The results obtained by the 2-D-C_s and 2-D-k models are similar, both in satisfactory agreement with the 3-D solution. However, as mentioned above, the 2-D-C_s model tends to underestimate the maximum bar heights of central bars but overestimate those of side bars, while the 2-D-k model consistently underestimates the maximum bar heights, as shown in Table 3, where the maximum bar heights predicted by the 3-D model are taken to be the basis for error assessment. The results given in Table 3 appear to indicate that the maximum bar heights predicted by the 2-D-C_s model are more accurate than those predicted by the 2-D-k model.

[26] In summary, the qualitative and quantitative comparisons made in sections 5.1.1 and 5.1.2 demonstrate that by incorporating the helical flow effect induced by streamline curvature the 2-D-C_s model gives satisfactory predictions of bed deformation, especially for the transverse component. Although *Repetto et al.* [2002] have previously made a correction for the effect of helical flow to modify their 2-D model and reached a similar conclusion, the outcomes associated with the simplified correction scheme used in the 2-D-C_s model demonstrate the utility of our approach over a 2-D-k model whose correction has to rely on the 3-D numerical solution. The credibility of our 2-D-C_s model is suitably justified, thus the model may well be used to predict a variety of forced bed forms that would develop under different combinations of parameter values.

5.2. Types of Forced Bars

[27] We present herein a classification system for forced bars induced by variations of channel width. Recall that *Repetto et al.* [2002] found that the wave number of width variations is the most important parameter on which the bed topography depends. For increasing values of λ_b, an increasing phase lag is found between bank profile and transverse bed configuration. However, our model results indicate that λ_b is not the only factor dominating such phase shift. Rather, the resulting bar pattern is a function of multiple factors (such as λ_b, θ_0, d_s, and β) that simultaneously act to influence its outcome, thus a variety of bed forms would develop under a given value of λ_b. Moreover, the width ratio β, which practically varies over a wide range for an observed value of λ_b, has long been seen as a basic control on the conditions for bed form development. Hence we choose to use β as a controlling parameter for classification of bar patterns. Variations of θ_0 and d_s, however, only influence the bar heights but not the bar patterns. The proposed approach is the first to classify the forced bars using the tractable locations of their peak deformations instead of using the intricate leading components of the Fourier representation of bed profile previously employed by *Repetto et al.* [2002].

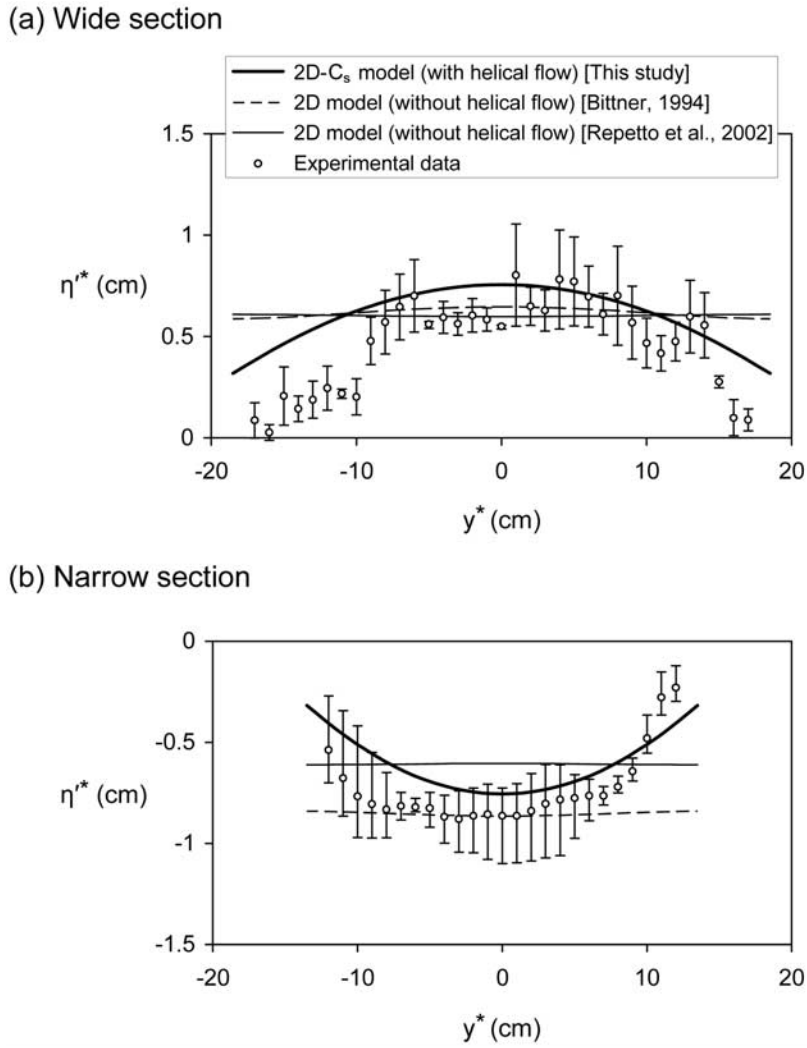

Figure 7. Transverse profiles of observed and predicted bed deformations at (a) wide and (b) narrow sections: run S-6 (this study) (λ_b = 0.3, θ_0 = 0.052, d_s = 0.035, β = 3.6).

[28] The bar patterns demonstrated by our model results can be classified into four types, namely, purely central bars, transverse bars of central mode 1, side bars, and transverse bars of central mode 2. Typical examples of these bar patterns are shown in Figure 12 using the gray-scale contour plots of η', where positive and negative values of η' (i.e., deposition and scour) are demonstrated with brighter and darker scales, respectively. Transition from one type to another is controlled by several variables but mainly the width ratio β. For increasing values of β, an increasing downstream shift of central bars is observed. For a smaller value of β (=2), purely central bars would form at the wide sections. As the value of β increases (=15), transverse bars would develop across the wide sections, with two lobes extending to upstream and peak deformations occurring at slightly downstream of the widest sections. This type of transverse bar and purely central bars are both classified as central bars of mode 1 because their peak values of η' occur at the centerline within region 1 (defined in Figure 1 as the region covering a 1/4 wavelength immediately downstream of the widest section). A further increase of β (=25) would result in formation of side bars at the wide sections. At a larger value of β (=50), transverse bars of the other kind would develop at upstream of the widest sections. Transverse bars of this kind are similar to transverse bars of central mode 1, but with an opposite orientation. This type of transverse bars is classified as central bars of mode 2 because their peak deformations occur at the centerline within region 2 (i.e., the region covering a 1/4 wavelength immediately upstream of the widest section). Among these four types of bar pattern, the first three have been observed in the laboratory flumes; however, the last one (i.e., transverse bars of central mode 2) was, to our best knowledge, never reported in the literature.

[29] The longitudinal profiles of η' along the centerline are demonstrated in Figure 13a for different types of forced bars. Deposition and scour occur near the wide (x = 0, 1, 2, 3) and narrow (x = 0.5, 1.5, 2.5) sections, respectively. The central bars of mode 1 and side bars have consistent trends of variation with β. For example, the amplitude of η' decreases with the increase of β, but the downstream shift of central bars increases with β. When it comes to the

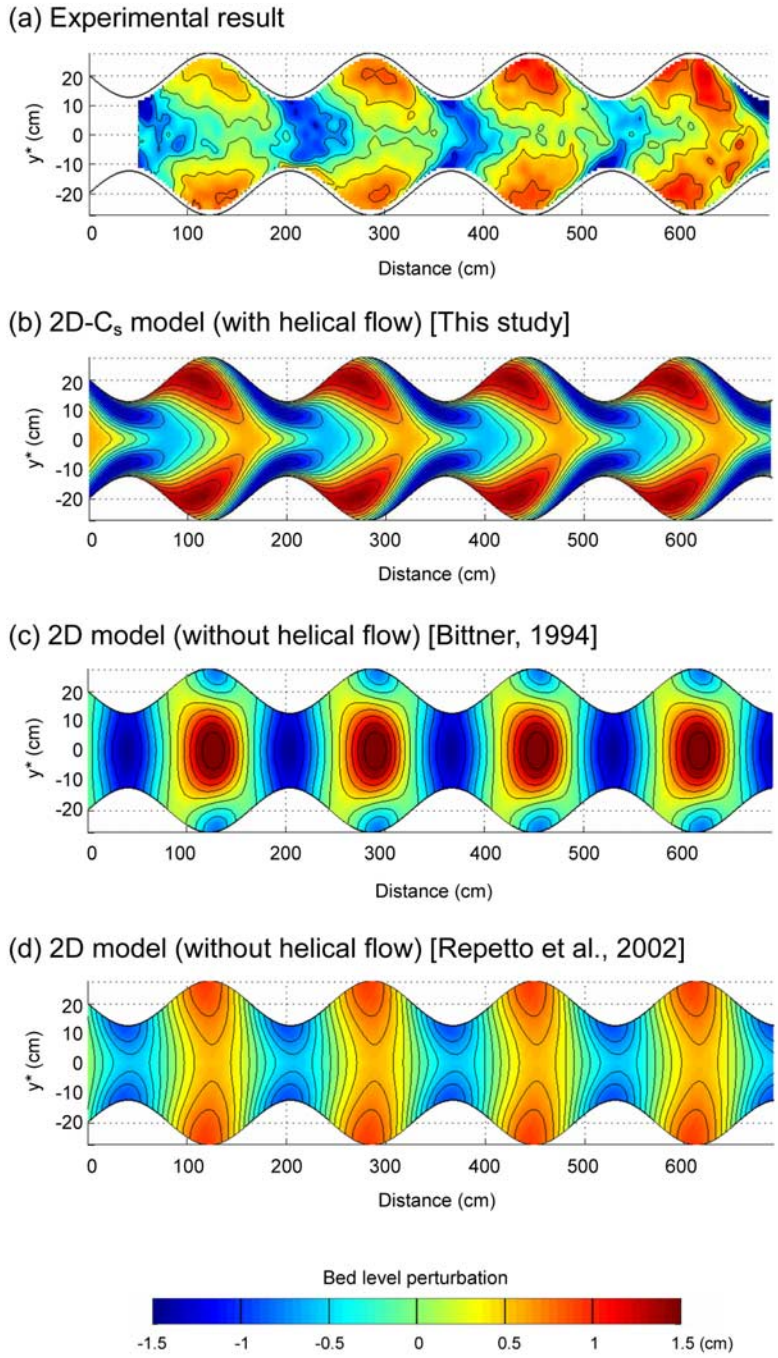

Figure 8. Contour plots showing (a) forced bars observed in run C1-11 [*Bittner*, 1994] and predicted results of (b) 2-D-C_s model (this study), (c) 2-D model [*Bittner*, 1994], and (d) 2-D model [*Repetto et al.*, 2002] ($\lambda_b = 0.8$, $\theta_0 = 0.102$, $d_s = 0.024$, $\beta = 9.1$).

central bars of mode 2, the amplitude of η' and the downstream shift of central bars become much greater. The transverse profiles of bed deformation are demonstrated in Figure 13b. For purely central bars, convex and concave profiles are observed at the wide and narrow sections, respectively. For transverse bars of central mode 1, flatter and wider profiles of depositions and scours are observed. For side bars, two peaks and troughs occur at both sides of the wide and narrow sections, respectively. The lateral profiles of the transverse bars of central mode 2 are, however, similar to those of side bars. The apparent discrepancies between the transverse bars of central modes 1 and 2 also indicate that a significant phase shift is associated with the latter.

6. Implications for Incipient Bifurcation

6.1. Mechanisms of Channel Bifurcation

[30] Channel bifurcations constitute one of the unit processes that govern the generation and development of a braided network. The laboratory observations made by *Ashmore* [1982, 1991] provided detailed descriptions of

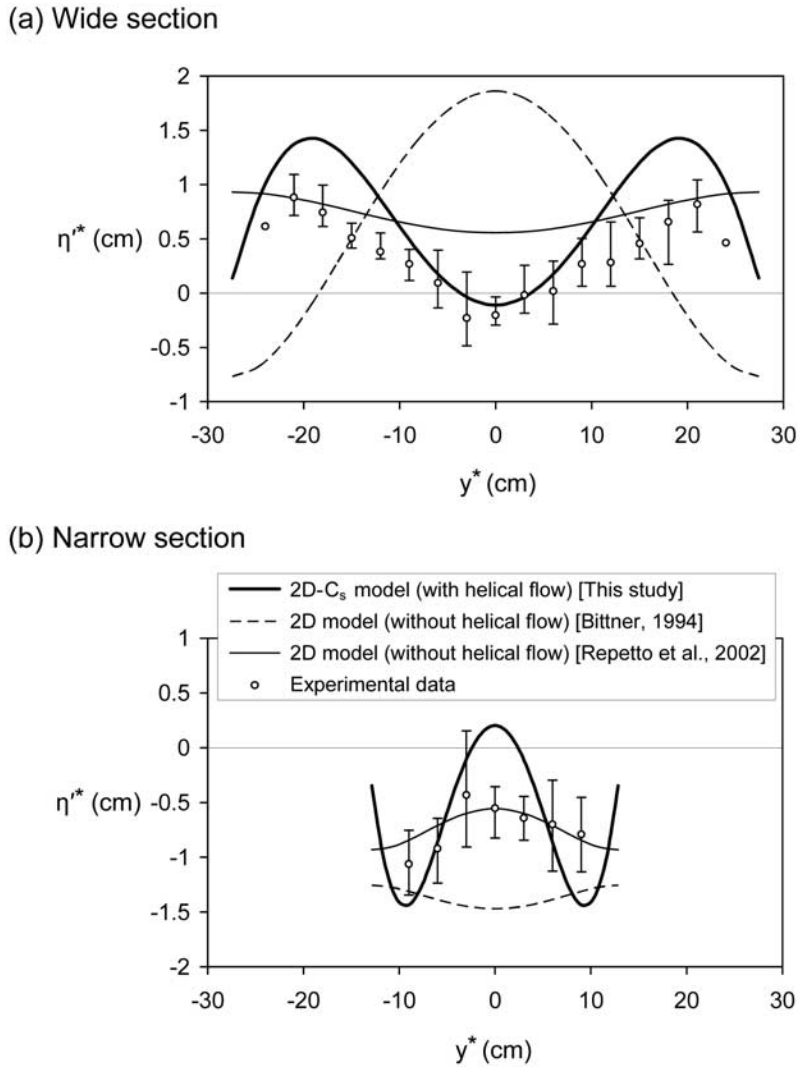

Figure 9. Transverse profiles of observed and predicted bed deformations at (a) wide and (b) narrow sections: run C1-11 [*Bittner*, 1994] (λ_b = 0.8, θ_0 = 0.102, d_s = 0.024, β = 9.1).

several unit processes, such as formation of alternate bars, channel bifurcations and confluences, incision of bars, avulsions, and channel migration. Among these, channel bifurcation is the formative process of fundamental importance for understanding the behavior of braided rivers [e.g., *Ferguson*, 1993; *Bolla Pittaluga et al.*, 2003]. The sensitive dependence of braided rivers on bifurcation conditions has been highlighted by *Hoey* [1992]. Channel bifurcations may be initiated with depositional or erosional processes [*Federici and Paola*, 2003]. *Ashmore* [1991] identified four possible mechanisms through which channel bifurcations may develop, two depositional and two erosional. The former include central bar deposition and transverse bar conversion; the latter include chute cutoff of point bars and dissection of multiple bars. Only depositional bifurcations are relevant to the present study, thus a brief description of their mechanisms is given below.

[31] Central bar deposition is a process in which an elongated, more or less symmetric, medial bar develops at the middle of a channel [e.g., *Ashmore*, 1991; *Ashworth*, 1996]. This mechanism, first described by *Leopold and Wolman* [1957], is the most commonly documented process of incipient braiding. The central bar initiation and growth are generally caused by the stalling of bed load sheets around the channel centerline due to the effect of streamline divergence, which has been confirmed experimentally by several investigators [e.g., *Ashworth*, 1996; *Federici and Paola*, 2003]. On the other hand, the medial bar may also be converted from a symmetric transverse unit bar [*Smith*, 1974; *Church and Jones*, 1982; *Ashmore*, 1991], whose downstream margin is usually marked by accumulation of coarser material. Bed load sheets are transported across the lateral margins of the transverse unit bar, but the central portion of the lee face stalls in the channel. Subsequent enlargement of the resulting medial bar occurs by lateral accretion and downstream extension. The presence of a submerged medial bar, initiated from either central bar deposition or transverse bar conversion, forces the flow to diverge and the bar nucleus is eventually exposed. The divided flows concentrate on both sides of the bar and

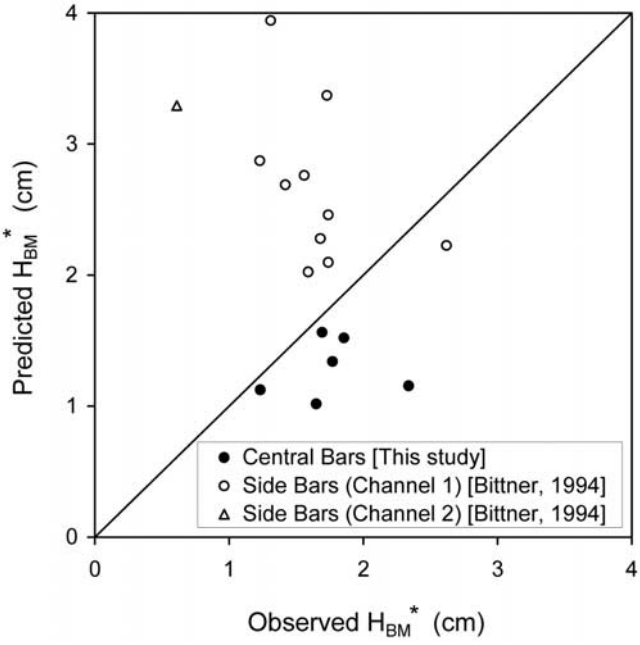

Figure 10. Comparison between observed and predicted maximum bar heights. Data include six central bars (this study) and 11 side bars [*Bittner*, 1994].

produce scour pools against both banks, thus induce widening of the channel and generation of a bifurcation.

6.2. Criteria for Incipient Bifurcation

[32] From the description given above, it becomes clear that depositional bifurcations develop as a consequence of flow division around the medial bars evolving from either central deposits or transverse unit bars. As such, formation of central bars may be viewed as a sign for incipient bifurcation, because such bed forms may induce the planimetric instability in a way that the flow enhances any small initial width variation leading to the generation of a bifurcation. Accordingly, the analytical solution obtained in section 3.2 may be used to establish a quantitative criterion for central bar formation, or equivalently, incipient bifurcation.

[33] For central bars of mode 1 to form in a channel (i.e., for central peaks to occur in region 1), the dimensionless bed deformation η' must satisfy the following conditions at $y = 0$:

$$\nabla\eta' = \left(\frac{\partial\eta'}{\partial x}, \frac{\partial\eta'}{\partial y}\right) = 0, \tag{25a}$$

$$\frac{\partial^2\eta'}{\partial x^2} < 0, \tag{25b}$$

$$\frac{\partial^2\eta'}{\partial x^2}\frac{\partial^2\eta'}{\partial y^2} - \left(\frac{\partial^2\eta'}{\partial x\partial y}\right)^2 > 0. \tag{25c}$$

Equation (25) assures that η' is a maximum value and the location of maximum η' is not a saddle point. Since η' is symmetric about x axis (e.g., see Figure 13b), $\partial\eta'/\partial y = 0$ is always true at $y = 0$ such that equation (25) can be simplified as

$$\frac{\partial\eta'}{\partial x} = 0, \tag{26a}$$

$$\frac{\partial^2\eta'}{\partial x^2} < 0, \tag{26b}$$

$$\frac{\partial^2\eta'}{\partial y^2} < 0. \tag{26c}$$

From equation (17), we have a linear expression for η', i.e.,

$$\eta' = \delta[\eta_1 \exp(i\lambda_b x) + \text{c.c.}] = 2\delta\text{Re}[\eta_1 \exp(i\lambda_b x)], \tag{27}$$

where $\eta_1 = H_1 - D_1$ is determined from (24), and can be expressed in the following form:

$$\eta_1 = f_1 + if_2, \tag{28}$$

in which $f_1 = \text{Re}[\eta_1]$ and $f_2 = \text{Im}[\eta_1]$ are both real functions of y. Then, equation (27) can be modified as

$$\eta' = 2\delta\,[f_1 \cos(\lambda_b x) - f_2 \sin(\lambda_b x)]. \tag{29}$$

The bank profile defined by equation (1) indicates that the values of sine and cosine are both positive in region 1. Based on this, we substitute equation (29) into (26) and obtain a final form of the criteria for central bar formation:

$$f_1 + \frac{f_2^2}{f_1} > 0 \tag{30a}$$

$$\frac{d^2 f_1}{dy^2} + \frac{d^2 f_2}{dy^2}\frac{f_2}{f_1} < 0. \tag{30b}$$

Equation (30) may be used to determine whether the central bars of mode 1 would develop (i.e., whether the condition of incipient bifurcation would occur) under a specific combination of λ_b, θ_0, d_s, and β.

[34] The criterion presented in (30) is different from that employed by *Repetto et al.* [2002], who followed the simplified approach classically proposed by *Ikeda et al.* [1981] to predict whether bank erosion tends to widen the channel where it is wider than the average, whereby the rate of bank retreat is related to the longitudinal excess velocity at the banks obtained numerically through the 3-D model. Here we choose to use the resulting bed form rather than the bank velocity as a criterion for predicting incipient bifurcation because the former has been suitably verified by flume experiments but the latter is potentially subject to considerable errors due to neglecting the no-slip boundary condition in solving the flow field. In fact, *Sun et al.* [2001] have pointed out that such flow solutions are only valid some distance away from the bank. According to the velocity distribution measured in our testing channel using the LDA

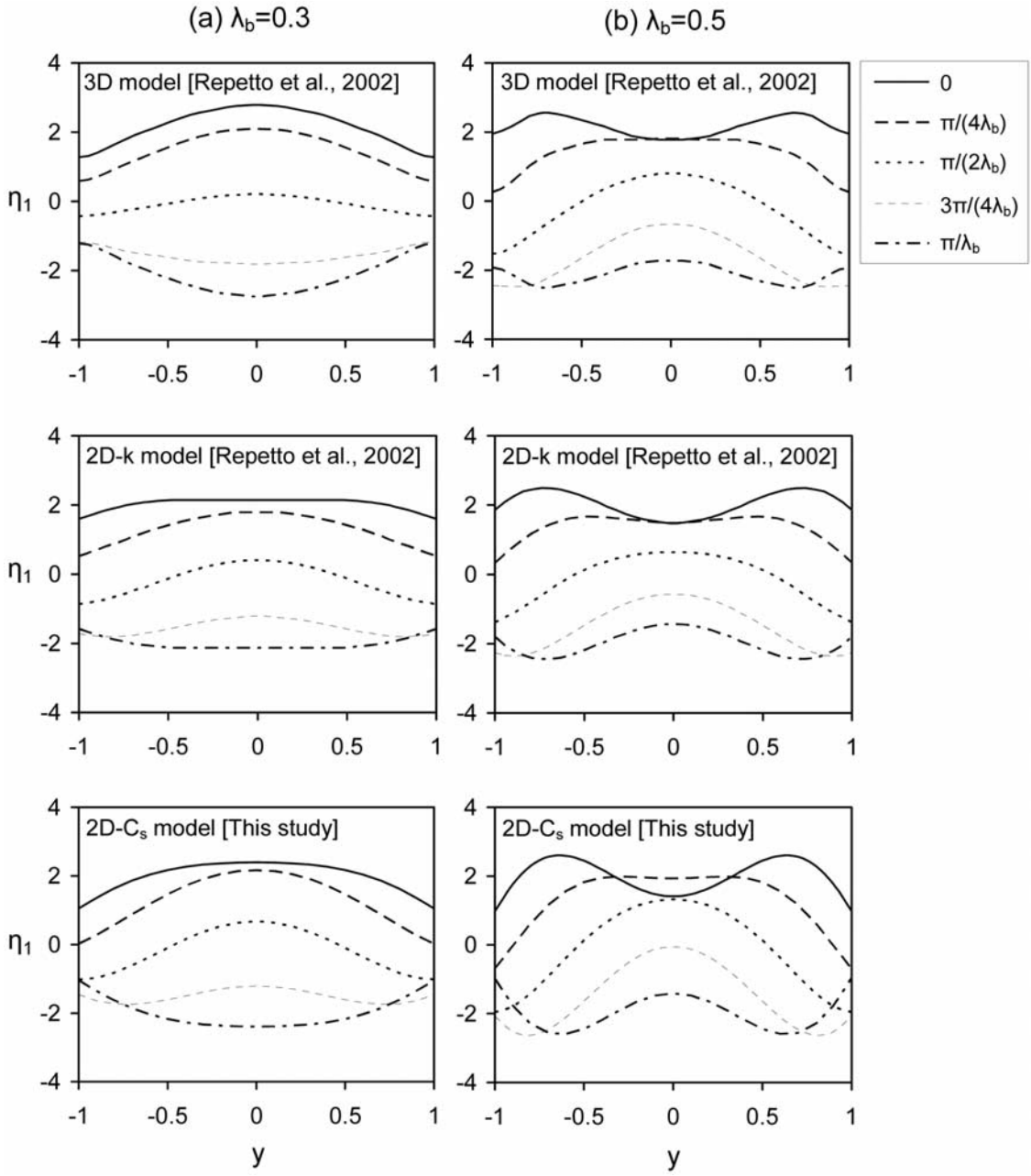

Figure 11. Transverse profiles of bed deformation at different values of x, obtained with three different models for (a) $\lambda_b = 0.3$ and (b) $\lambda_b = 0.5$ ($\theta_0 = 0.1$, $d_s = 0.05$, $\beta = 10$).

(laser Doppler anemometer), we found that the longitudinal velocities measured along a transverse section agree well with the predicted results in the central (off-bank) region but deviate from the analytical solution in the near-bank region, where the measured velocities are much smaller than the calculated values. This is especially apparent for the narrow section, where the model predicts the near-bank velocities to be greater than the off-bank velocities, which is clearly against reality. In our 2-D-C_s model, although the bed deformations are based on such distorted near-bank velocities, the resulting overall bed form (or bar pattern) is generally satisfactory. In other words, by relaxing the no-slip condition the model gives distorted velocities and bed deformations only in the near-bank region. For the major part of the channel, the flow field is, however, reasonably accurate and the resulting bed topography is useful for predicting incipient bifurcation.

[35] For a given combination of λ_b, θ_0, and d_s, we found that the criteria given by (30) are satisfied for a range of β. When the value of β is smaller than a lower critical value

Table 3. Comparison of Maximum Bar Heights Predicted by Different Models

Model	Dimensionless Maximum Bar Height H_{BM}	
	Central Bars ($\lambda_b = 0.3$)	Side Bars ($\lambda_b = 0.5$)
3-D model [*Repetto et al.*, 2002]	5.53 (base value)	5.07 (base value)
2-D-*k* model [*Repetto et al.*, 2002]	4.27 (−23% error)	4.94 (−3% error)
2-D-C_s model (this study)	4.79 (−13% error)	5.22 (+3% error)

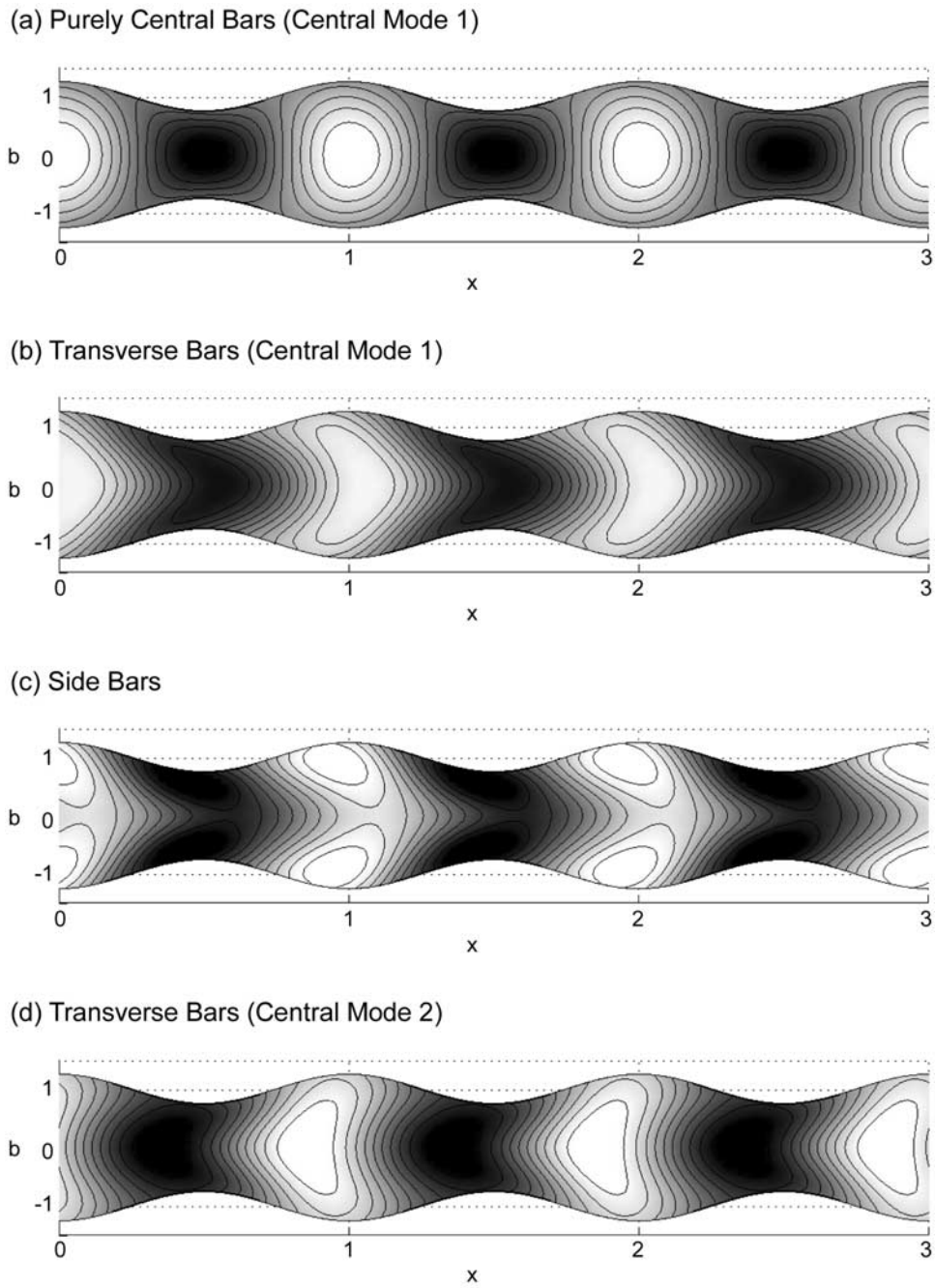

Figure 12. Gray-scale contour plots of dimensionless bed deformation η' for different types of forced bars: (a) purely central bars ($\lambda_b = 0.3$, $\theta_0 = 0.1$, $d_s = 0.01$, $\beta = 2$); (b) transverse bars of central mode 1 ($\lambda_b = 0.3$, $\theta_0 = 0.1$, $d_s = 0.01$, $\beta = 15$); (c) side bars ($\lambda_b = 0.3$, $\theta_0 = 0.1$, $d_s = 0.01$, $\beta = 25$); and (d) transverse bars of central mode 2 ($\lambda_b = 0.3$, $\theta_0 = 0.1$, $d_s = 0.2$, $\beta = 50$). Positive and negative values of η' (i.e., deposition and scour) are demonstrated with brighter and darker scales, respectively.

β_{c1}, the criteria given by (30) are satisfied and thus the central bars of mode 1 would develop. As the value of β exceeds β_{c1}, the criteria are violated and side bars would form in the channel. If the value of β continues to increase and exceeds an upper critical value β_{c2}, the central bars of mode 2 would be present. For illustration, a contour plot of β_{c1} corresponding to our experimental setting ($\lambda_b = 0.3$) and typical ranges of θ_0 and d_s is presented in Figure 14a. The values of β_{c1} cover a range roughly between 8 and 22, with the largest values occurring at moderate θ_0 ($0.08 \sim 0.14$) and larger d_s ($0.07 \sim 0.2$). The values of β_{c1} corresponding to the experimental setting ($\lambda_b = 0.8$) of *Bittner* [1994] are, however, all very close to 0 over these typical ranges of θ_0 and d_s, thus are not shown here. Alternatively, the contour plot of β_{c2} is demonstrated in Figure 14b, where the values of β_{c2} cover a range roughly between 8 and 20, with the largest values occurring at smallest d_s (<0.02). Given flow and sediment conditions, these contour plots may be used to determine β_{c1} and β_{c2} below which central and side bars would form in the channel, respectively.

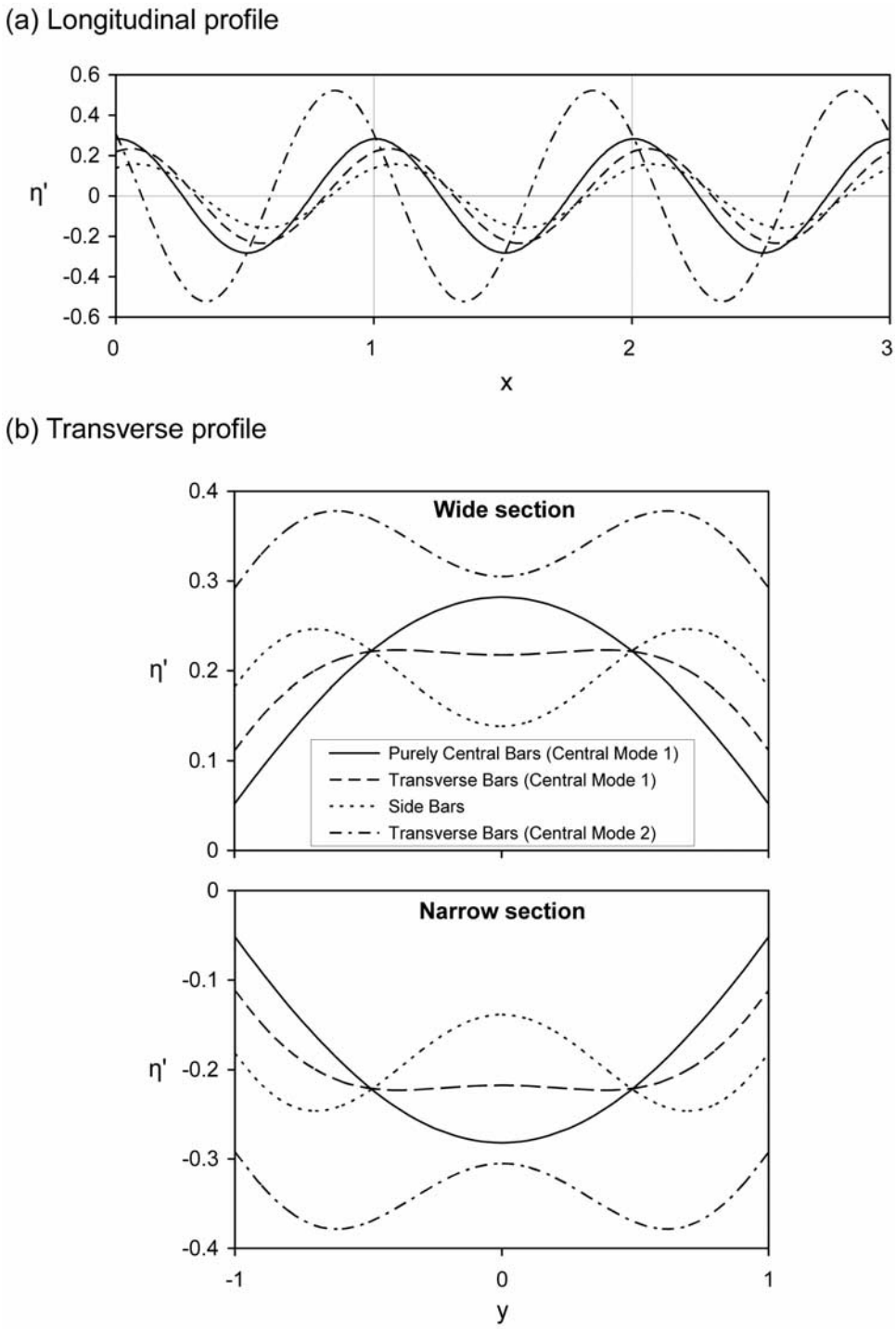

Figure 13. (a) Longitudinal profiles of dimensionless bed deformation η' at the centerline. (b) Transverse profiles of dimensionless bed deformation η' at the wide and narrow sections. These forced bars are identical to those shown in Figure 12.

[36] To check if the proposed criteria would result in correct predictions of bar pattern, two sets of experimental data, one from this study and the other from *Bittner* [1994], are employed herein. The former include 10 observed central bars and 2 side bars (see Table 2), the latter include 11 side bars observed in two different channels. The results are demonstrated in Figure 15, where the observed values of β are compared with the corresponding critical values. It is found that the observed bar patterns all coincide with the predicted bed forms (i.e., central bars of mode 1 and side bars in Figures 15a and 15b), indicating that the proposed criteria may provide credible predictions of bar pattern. The corresponding results predicted with the criterion of *Repetto et al.* [2002] are also shown in Table 4, where their approach correctly predicts formation of side bars but fails to predict those central bars observed at relatively small

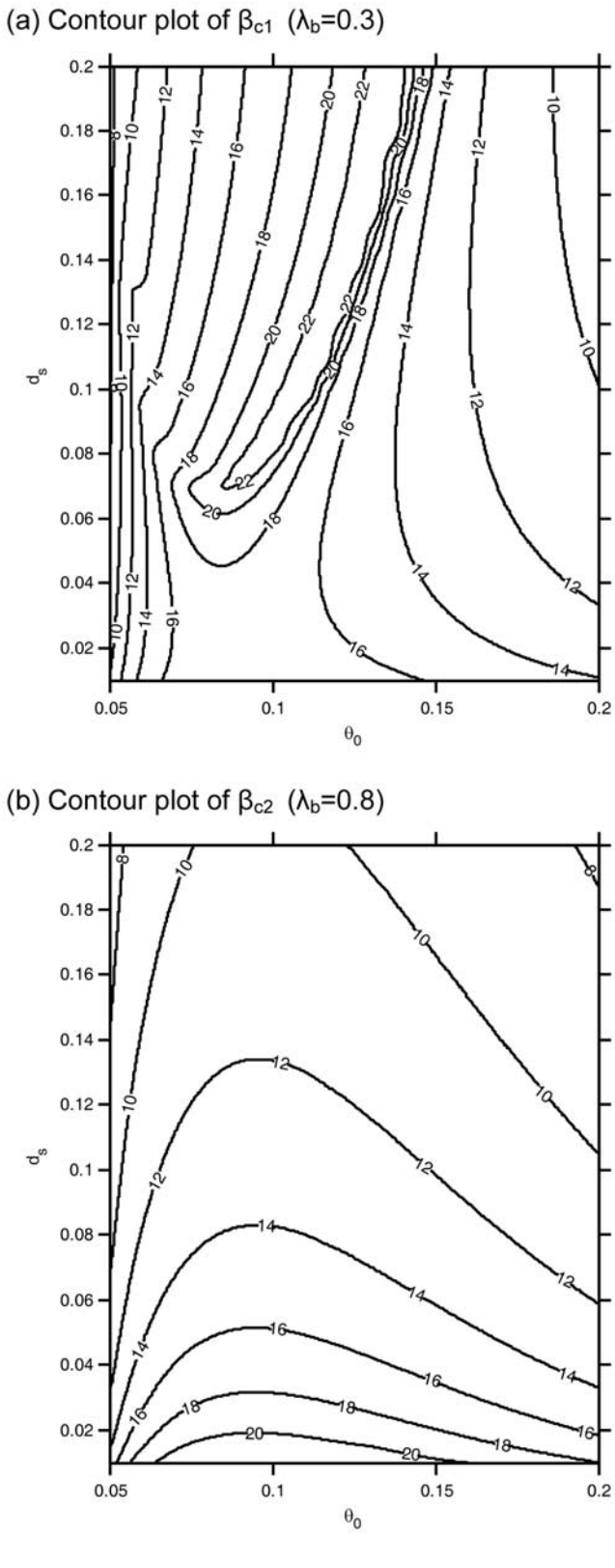

Figure 14. Contour plots showing (a) lower critical values β_{c1} for $\lambda_b = 0.3$ and (b) upper critical values β_{c2} for $\lambda_b = 0.8$, both corresponding to typical ranges of θ_0 and d_s.

values of β. A possible reason for this is that the longitudinal excess velocity at the banks is adopted as a criterion for predicting planimetric instability. As mentioned earlier, due to the relaxed no-slip condition, considerable error is associated with the predicted near-bank velocities particularly for narrow channels. *Repetto et al.* [2002] pointed out that such a simplified treatment would always lead to a negative value for the real part of the longitudinal excess velocity at the banks, and thus a prediction of side bars at those small values of β.

[37] To further test the proposed criteria at a larger value of β (=15), the theoretical findings are extracted from the work of *Repetto et al.* [2002] for two different λ_b values (0.3 and 0.8). For $\lambda_b = 0.3$, *Repetto et al.* [2002] predicted formation of central bars at $\theta_0 = 0.08$ and 0.1, whereas side bars were predicted to develop at $\theta_0 = 0.06$, 0.15, 0.2 and 0.3 (for $d_s = 0.1$). The corresponding bed forms predicted by our criteria agree with the findings of *Repetto et al.* [2002] (Figure 15a and Table 4). For $\lambda_b = 0.8$, the theoretical findings of *Repetto et al.* [2002] are invariably side bars,

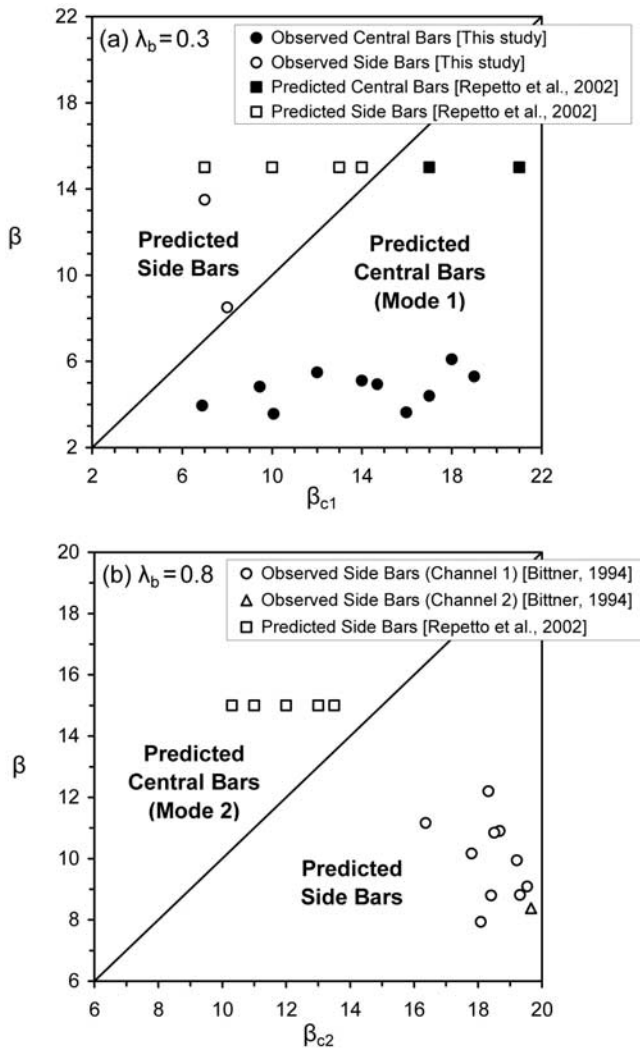

Figure 15. Comparisons between observed values of β and corresponding values of (a) β_{c1} (for $\lambda_b = 0.3$) and (b) β_{c2} (for $\lambda_b = 0.8$). Boldface indicates the regions of predicted bar pattern.

Table 4. Comparison Between Observed and Predicted Bed Forms[a]

Source of Data	Observed Bed Form	Predicted Bed Form	
		Using Criteria Presented in this Study	Using Criteria Proposed by *Repetto et al.* [2002]
This study ($\lambda_b = 0.3$)	central bars (mode 1)[b]	**central bars (mode 1)**	**side bars** (incorrect prediction)
	side bars[c]	side bars	side bars
Repetto et al. [2002][d] ($\lambda_b = 0.3$)	. . .	central bars (mode 1)	central bars
	. . .	side bars	side bars
Bittner [1994][e] ($\lambda_b = 0.8$)	side bars	side bars	side bars
Repetto et al. [2002][f] ($\lambda_b = 0.8$)	. . .	**central bars (mode 2)**	**side bars**

[a]Boldface indicates that bed forms predicted by the two criteria are conflicting.
[b]$\theta_0 = 0.047 \sim 0.103$; $d_s = 0.035 \sim 0.06$; $\beta = 3.6 \sim 6.1$.
[c]$\theta_0 = 0.046 \sim 0.051$; $d_s = 0.084 \sim 0.133$; $\beta = 8.5 \sim 13.5$.
[d]$\theta_0 = 0.06 \sim 0.3$; $d_s = 0.1$; $\beta = 15$.
[e]$\theta_0 = 0.056 \sim 0.138$; $d_s = 0.021 \sim 0.032$; $\beta = 7.9 \sim 12.2$.
[f]$\theta_0 = 0.06 \sim 0.2$; $d_s = 0.1$; $\beta = 15$.

conflicting with our predictions, i.e., the central bars of mode 2 (Figure 15b and Table 4). *Repetto et al.* [2002] found that the forced bar pattern is strongly dependent upon the wave number of width variations, such that for given values of β and θ_0 a threshold value of λ_b exists above which the resulting bed form is always side bars (in this case the threshold value would be 0.33). Our model results, however, indicate that the final bed form is dependent upon a combination of multiple factors instead of one single factor, and here the central bars of mode 2 would develop for $\beta > \beta_{c2}$. Since neither of these predictions for $\lambda_b = 0.8$ is supported by laboratory observations, it remains as an open problem for future studies.

[38] From above, we found that the predictions obtained using our criterion and that of *Repetto et al.* [2002] are not fully consistent. Here the merit of using our approach to predict the forced bar patterns and thus the conditions of incipient bifurcation is further elucidated. *Repetto et al.* [2002] reported that the conditions under which the perturbed flow produces a positive erosion rate at the wide section, implying incipient bifurcation of a channel, are strictly connected with the transverse deformations of flow and bed topography associated with the 3-D effects. Thus even though the cross-sectional average velocity attains its maximum close to the narrowest section, it is possible that the velocity and shear stress at the banks peak where the channel is wider than the average. In the latter situation the planform is unstable, as bank erosion tends to enhance the initially small width perturbation. However, according to the results of their 2-D model (without helical flow), *Repetto et al.* [2002] found that the planform would be invariably stable since the longitudinal bank velocity always attains its maximum value close to the narrowest section. In this regard, their 3-D model may result in a more accurate flow field that includes the helical flows, but without considering the no-slip boundary condition the near-bank velocities could still be subject to considerable errors. Therefore we believe that it is more reasonable to use the suitably justified bed topography resulting from the 2-D-C_s model with only minor distortions being present near the banks, but not to use the distorted bank velocity itself, as a criterion for predicting planimetric instability.

[39] As observed in our experiments, the final bed forms were extremely sensitive to boundary disturbances as well as the instabilities associated with turbulent flows and sediment transport. To create stable regimes in which only forced bars are present, we had to use small values of β; special efforts were also made to minimize boundary disturbances. In most situations, alternate bars and forced bars would coexist in the channel. For example, 9 out of 15 runs performed in this study were associated with alternate bars, while among the 23 runs of *Bittner* [1994] there were 12 unstable runs in which alternate bars developed. The threshold conditions for formation of alternate bars, as addressed by *Colombini et al.* [1987], are beyond the scope of this study. The proposed critical values of β corresponding to the central and side bars are, however, necessary conditions for formation of these forced bed forms but not sufficient conditions for establishing stable regimes. Braiding generally develops in channels where alternate bars are frequent and bar migration is ubiquitous. It also occurs in channels whose aspect ratios are typically much greater than those under which central bars formed in our channel. The central bars observed in our experiments offer useful data for verification of model results under stable regimes; the proposed criterion provides credible predictions of forced bed forms and useful implications for incipient bifurcation. However, it should be noted that the unstable regimes in which alternate and forced bars coexist are probably more relevant to the field processes of channel braiding.

7. Conclusions

[40] In this study we found that by relaxing the no-slip condition at the banks, the 2-D-C_s model gives distorted bed deformations in the near-bank region. For the major part of the channel, the flow field is, however, reasonably accurate and the resulting bed topography is satisfactory. The 2-D-C_s model tends to overestimate the maximum bar heights of side bars, but underestimate those of central bars. The forced bed forms are classified into four different bar types based on their locations of peak deformations. Transition from one type to another is controlled by several variables but especially the width ratio β. For increasing values of β, central bars will shift downstream, leading sequentially to the patterns of purely central bars, transverse bars of central mode 1, side bars, and transverse bars of central mode 2. Among these bed forms, the transverse bars of central mode 2 were never observed in the flume tests, thus remain to be confirmed experimentally.

[41] The criteria for central bar formation, implying a condition required for incipient bifurcation, are derived

analytically using the linear solution of bed deformation. Given λ_b, θ_0, and d_s, the central bars of mode 1 would develop for $\beta < \beta_{c1}$, the central bars of mode 2 would form for $\beta > \beta_{c2}$, whereas side bars would be present for $\beta_{c1} < \beta < \beta_{c2}$. The bed forms predicted by these criteria coincide with the observed bar patterns. The approach proposed by *Repetto et al.* [2002] based on the bank velocity fails to predict the observed central bars at small values of β. For large values of λ_b and β, their approach invariably predicts formation of side bars, which conflict with the central bars of mode 2 predicted by our criteria. The outcomes demonstrate the merit of using the resulting bed topography that is overall satisfactory but distorted only near the banks, instead of using the distorted bank velocity itself, as a criterion for predicting planimetric instability. However, the proposed criteria for formation of different bar patterns are necessary but not sufficient conditions for establishing stable regimes. Braiding generally develops in channels where alternate and forced bars coexist; in that sense the unstable regimes are probably more relevant to field processes. As such, the nonlinear interactions between free and forced bars need to be resolved in the future. In addition, the effects of mixed grain sizes and partial transport [*Wu and Yang*, 2004] in gravel bed rivers may also be incorporated into future studies.

Notation

A dimensionless amplitude of width variations.
a a coefficient for the effect of streamline curvature.
$a_1 \sim a_{10}$ coefficients defined in equation (20).
B_0^* average half-width of the channel.
b dimensionless local half-width of the channel.
b' perturbed term of b.
b^* local half-width of the channel.
C_f friction coefficient.
C_{f0} friction coefficient of reference uniform flow.
C_s dimensionless local curvature of streamline.
D dimensionless water depth.
D' perturbed term of D.
D^* water depth.
D_1 linear solution of D'.
D_0^* average depth of reference uniform flow.
d_s dimensionless sediment diameter.
d_s^* sediment diameter.
F_0 Froude number of reference uniform flow.
f_1 real part of η_1.
f_2 imaginary part of η_1.
g gravitational acceleration.
H dimensionless water level.
H' perturbed term of H.
H^* water level.
H_{BM} dimensionless maximum bar height ($=H_{BM}^*/D_0^*$).
H_0 dimensionless local water level of reference uniform flow.
H_1 linear solution of H'.
H_{BM}^* maximum bar height.
H_0^* local mean water level of reference uniform flow.
L_b^* wavelength of width variations.
(q_x, q_y) dimensionless sediment transport vector.
(q_x^*, q_y^*) sediment transport vector per unit width.
R density difference ratio = $(\rho_s - \rho)/\rho$.
r a coefficient for transverse bed gradient.
S channel slope.
$s_1 \sim s_3$ coefficients defined in equation (20).
(U, V) dimensionless velocity vector.
(U', V') perturbed terms of (U, V).
(U^*, V^*) velocity vector.
(U_1, V_1) linear solutions of (U', V').
U_0^* average velocity of reference uniform flow.
V_s corrected dimensionless transverse velocity.
x dimensionless longitudinal coordinate.
x^* longitudinal coordinate.
y dimensionless transverse coordinate.
y^* transverse coordinate.
α angle between average particle path and x^* axis.
β average aspect (or width to depth) ratio = B_0^*/D_0^*.
β_{c1} a lower critical aspect ratio.
β_{c2} an upper critical aspect ratio.
$\Gamma_0 \sim \Gamma_3$ coefficients defined in equation (22).
γ specific weight of water.
$\gamma_1 \sim \gamma_8$ coefficients defined in equations (23) and (24).
χ angle between directions of local shear stress and x^* axis.
δ a small perturbation of channel width ($=A/2$).
Φ dimensionless bed load intensity function.
Φ_0 bed load intensity of reference uniform flow ($=q_{x0}$).
θ dimensionless bed shear stress (Shields parameter).
θ_c dimensionless critical shear stress.
θ_0 dimensionless shear stress of reference uniform flow.
ρ, ρ_s water and sediment densities.
η dimensionless bed level.
η' perturbed term of η.
η'^* bed level perturbation ($=\eta' D_0^*$).
η_1 linear solution of η'.
λ_b dimensionless wave number of width variations.
λ_1, λ_2 coefficients defined in equation (23).
λ_b^* wave number of width variations $=2\pi/L_b^*$.
τ^* local bed shear stress.
τ_0^* bed shear stress of reference uniform flow.
(τ_x, τ_y) dimensionless bed stress vector.
(τ_x^*, τ_y^*) bed shear stress vector.

[42] **Acknowledgments.** This study was granted with the Young Investigator Research Award of National Science Council, Taiwan. The authors acknowledge H. Capart (NTU) for the DTM scanning technology. Critical comments from two anonymous reviewers helped improve this paper significantly.

References

Ashmore, P. E. (1982), Laboratory modeling of gravel bed stream morphology, *Earth Surf. Processes Landforms*, *7*, 201–225.
Ashmore, P. E. (1991), How do gravel-bed rivers braid?, *Can. J. Earth Sci.*, *28*, 326–341.
Ashworth, P. J. (1996), Mid-channel bar growth and its relationship to local flow strength and direction, *Earth Surf. Processes Landforms*, *21*, 103–123.
Bittner, L. D. (1994), River bed response to channel width variation: Theory and experiments, M.S. thesis, Univ. of Ill., Urbana-Champaign.
Blondeaux, P., and G. Seminara (1985), A unified bar-bend theory of river meanders, *J. Fluid Mech.*, *157*, 449–470.

Bolla Pittaluga, M., R. Repetto, and M. Tubino (2003), Channel bifurcation in braided rivers: Equilibrium configurations and stability, *Water Resour. Res.*, *39*(3), 1046, doi:10.1029/2001WR001112.

Callander, R. A. (1969), Instability and river channels, *J. Fluid Mech.*, *36*, 465–480.

Callander, R. A. (1978), River meandering, *Annu. Rev. Fluid Mech.*, *10*, 129–158.

Chien, N. (1956), The present status of research on sediment transport, *Trans. Am. Soc. Civ. Eng.*, *121*, 833–844.

Church, M., and D. Jones (1982), Channel bars in gravel-bed rivers, in *Gravel-Bed Rivers*, edited by R. D. Hey, J. C. Bathurst, and C. R. Thorne, pp. 291–324, John Wiley, Hoboken, N. J.

Colombini, M., G. Seminara, and M. Tubino (1987), Finite-amplitude alternate bars, *J. Fluid Mech.*, *181*, 213–232.

Darby, S. E., A. M. Alabyan, and M. J. Van de Wiel (2002), Numerical simulation of bank erosion and channel migration in meandering rivers, *Water Resour. Res.*, *38*(9), 1163, doi:10.1029/2001WR000602.

de Vriend, H. J. (1981), Velocity redistribution in curved rectangular channels, *J. Fluid Mech.*, *107*, 423–439.

Engelund, F. (1974), Flow and bed topography in channel bends, *J. Hydraul. Div. Am. Soc. Civ. Eng.*, *100*, 1631–1648.

Federici, B., and C. Paola (2003), Dynamics of channel bifurcations in noncohesive sediments, *Water Resour. Res.*, *39*(6), 1162, doi:10.1029/2002WR001434.

Ferguson, R. I. (1993), Understanding braiding processes in gravel-bed rivers: Progress and unsolved problems, *Spec. Publ. Geol. Soc.*, *75*, 73–87.

García, M., and Y. Niño (1993), Dynamics of sediment bars in straight and meandering channels: Experiments on the resonance phenomenon, *J. Hydraul. Res.*, *31*, 739–761.

Hoey, T. (1992), Temporal variations in bedload transport rates and sediment storage in gravel-bed rivers, *Prog. Phys. Geogr.*, *16*, 319–338.

Ikeda, S. (1982), Lateral bed load transport on side slopes, *J. Hydraul. Div. Am. Soc. Civ. Eng.*, *108*, 1369–1373.

Ikeda, S., and T. Nishimura (1985), Bed topography in bends of sand-silt rivers, *J. Hydraul. Eng.*, *111*, 1397–1411.

Ikeda, S., G. Parker, and K. Sawai (1981), Bend theory of river meanders, part 1, Linear development, *J. Fluid Mech.*, *112*, 363–377.

Johannesson, H., and G. Parker (1989a), Secondary flow in mildly sinuous channel, *J. Hydraul. Eng.*, *115*, 289–308.

Johannesson, H., and G. Parker (1989b), Linear theory of river meanders, in *River Meandering*, *Water Resour. Monogr. Ser.*, vol. 12, edited by S. Ikeda and G. Parker, pp. 181–213, AGU, Washington, D. C.

Kalkwijk, J. P. T., and H. J. de Vriend (1980), Computation of the flow in shallow river bends, *J. Hydraul. Res.*, *18*, 327–342.

Kikkawa, H., S. Ikeda, and A. Kitagawa (1976), Flow and bed topography in curved open channels, *J. Hydraul. Div. Am. Soc. Civ. Eng.*, *102*, 1327–1342.

Kinoshita, R., and H. Miwa (1974), River channel formation which prevents downstream translation of transverse bars (in Japanese), *Shinsabo*, *94*, 12–17.

Kitanidis, P. K., and J. F. Kennedy (1984), Secondary current and river-meander formation, *J. Fluid Mech.*, *144*, 217–229.

Leopold, L. B., and M. G. Wolman (1957), River channel patterns, braided, meandering, and straight, *U.S. Geol. Surv. Prof. Pap., 282-B*.

Leschziner, M. A., and W. Rodi (1979), Calculation of strongly curved open channel flow, *J. Hydraul. Div. Am. Soc. Civ. Eng.*, *105*, 1297–1314.

Parker, G. (1990), Surface-based bedload transport relation for gravel rivers, *J. Hydraul. Res.*, *20*, 417–436.

Parker, G., and H. Johannesson (1989), Observations on several recent theories of resonance and overdeepening in meandering channels, in *River Meandering*, *Water Resour. Monogr. Ser.*, vol. 12, edited by S. Ikeda and G. Parker, pp. 379–415, AGU, Washington, D. C.

Repetto, R. (2000), Unit processes in braided rivers, Ph.D. thesis, Univ. of Genova, Italy.

Repetto, R., M. Tubino, and C. Paola (2002), Planimetric instability of channels with variable width, *J. Fluid Mech.*, *457*, 79–109.

Seminara, G., and M. Tubino (1989), Alternate bars and meandering: Free, forced and mixed interactions, in *River Meandering*, *Water Resour. Monogr. Ser.*, vol. 12, edited by S. Ikeda and G. Parker, pp. 267–320, AGU, Washington, D. C.

Seminara, G., G. Zolezzi, M. Tubino, and D. Zardi (2001), Downstream and upstream influence in river meandering, part 2, Planimetric development, *J. Fluid Mech.*, *438*, 213–230.

Smith, N. D. (1974), Sedimentology and bar formation in the upper Kicking Horse River, a braided meltwater stream, *J. Geol.*, *82*, 205–224.

Spinewine, B., H. Capart, M. Larcher, and Y. Zech (2003), Three-dimensional Voronoï imaging methods for the measurement of near-wall particulate flows, *Exper. Fluids*, *34*, 227–241.

Sun, T., P. Meakin, and T. Jøssang (2001), A computer model for meandering rivers with multiple bed load sediment sizes: 1. Theory, *Water Resour. Res.*, *37*, 2227–2241.

Talmon, A. M., N. Struiksma, and M. C. L. M. Van Mierlo (1995), Laboratory measurements of the direction of sediment transport on transverse alluvial-bed slopes, *J. Hydraul. Res.*, *33*, 519–534.

Tubino, M., and G. Seminara (1990), Free-forced interactions in developing meanders and suppression of free bars, *J. Fluid Mech.*, *214*, 131–159.

Tubino, M., R. Repetto, and G. Zolezzi (1999), Free bars in rivers, *J. Hydraul. Res.*, *37*, 759–775.

Whiting, P. J., and W. E. Dietrich (1993), Experimental studies of bed topography and flow patterns in large-amplitude meanders: 1. Observations, *Water Resour. Res.*, *29*, 3605–3614.

Wilcock, P. R. (1998), Two-fraction model of initial sediment motion in gravel-bed rivers, *Science*, *280*, 410–412.

Wu, F.-C., and Y.-J. Chou (2003), Simulation of gravel-sand bed response to flushing flows using a two-fraction entrainment approach: Model development and flume experiment, *Water Resour. Res.*, *39*(8), 1211, doi:10.1029/2003WR002184.

Wu, F.-C., and K.-H. Yang (2004), A stochastic partial transport model for mixed-size sediment: Application to assessment of fractional mobility, *Water Resour. Res.*, *40*, W04501, doi:10.1029/2003WR002256.

Wu, F.-C., and T.-H. Yeh (2004), Nonlinear analysis of forced bars in variable-width channels, *Eos Trans. AGU*, *85*(28), West. Pac. Geophys. Meet. Suppl., Abstract H33A-75.

F.-C. Wu and T.-H. Yeh, Department of Bioenvironmental Systems Engineering, National Taiwan University, No 1, Sec 4, Roosevelt Road, Taipei, Taiwan. (fcwu@ntu.edu.tw)